Insights on spin delocalization and spin polarization mechanisms in crystals of azido copper(II) dinuclear complexes through the electron spin density Source Function

Carlo Gatti,[a]* Giovanni Macetti[b] and Leonardo Lo Presti[b]

[a]CNR–ISTM Istituto di Scienze e Tecnologie Molecolari, via Golgi 19, I-20133 Milano, Italy, and [b]Department of Chemistry, Università degli Studi di Milano, via Golgi 19, I-20133 Milano, Italy. *Correspondence e-mail: c.gatti@istm.cnr.it

The Source Function (SF) tool was applied to the analysis of the *theoretical* spin density in azido Cu^{II} dinuclear complexes, where the azido group, acting as a coupler between the Cu^{II} cations, is linked to the metal centres either in an end-on or in an end–end fashion. Results for only the former structural arrangement are reported in the present paper. The SF highlights to which extent the magnetic centres contribute to determine the local spin delocalization and polarization at any point in the dimetallic complex and whether an atom or group of atoms of the ligands act in favour or against a given local spin delocalization/polarization. Ball-and-stick atomic SF percentage representations allow for a visualization of the magnetic pathways and of the specific role played by each atom along these paths, at given reference points. Decomposition of SF contributions in terms of a magnetic and of a relaxation component provides further insight. Reconstruction of partial spin densities by means of the Source Function has for the first time been introduced. At variance with the standard SF percentage representations, such reconstructions offer a simultaneous view of the sources originating from specific subsets of contributing atoms, in a selected molecular plane or in the whole space, and are therefore particularly informative. The SF tool is also used to evaluate the accuracy of the analysed spin densities. It is found that those obtained at the unrestricted B3LYP DFT level, relative to those computed at the CASSCF(6,6) level, greatly overestimate spin delocalization to the ligands, but comparatively underestimate magnetic connection (*spin transmission*) among atoms, along the magnetic pathways. As a consequence of its excessive spin delocalization, the UB3LYP method also overestimates spin polarization mechanisms between the paramagnetic centres and the ligands. Spin delocalization measures derived from the refinement of Polarized Neutron Diffraction data seem in general superior to those obtained through the DFT UB3LYP approach and closer to the far more accurate CASSCF results. It is also shown that a visual agreement on the spin-resolved electron densities ρ_α and ρ_β derived from different approaches does not warrant a corresponding agreement between their associated spin densities.
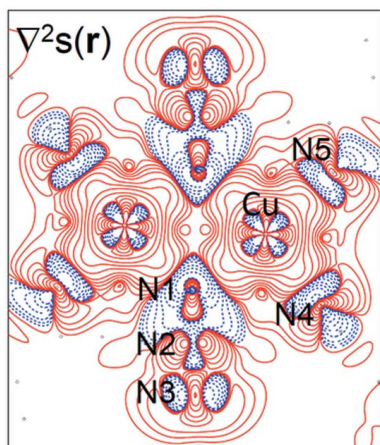
1. Introduction

Electron distributions are quantum mechanical observables and scattering techniques enable their model reconstruction in crystalline solids (Coppens, 1997). Focusing on the real space representation of such distributions, X-ray and electron diffraction lead to the crystalline electron position density $\rho(\mathbf{r})$, while its spin counterpart, $s(\mathbf{r})$, may be derived from polarized neutron diffraction (PND) experiments on magnetic crystals (Gillon & Becker, 2012).

During the last 50 years, Philip Coppens has played a pivotal role in developing techniques to derive increasingly

$\nabla^2 s(\mathbf{r})$

N5
Cu
N1
N2
N3
N4

© 2017 International Union of Crystallography

accurate X-ray electron densities and in popularizing their use through several landmark papers (for a summary, see Coppens, 2015; Koritsanszky & Coppens, 2001) and the comprehensive book on *X-ray Charge Densities and Chemical Bonding* (Coppens, 1997). Thanks to him and to many other practitioners, the field could develop so strongly to make him feel confident enough, in 2009, to write a short report in *Angewandte Chemie* entitled *Charge Densities Come of Age* (Coppens, 2009). If his view may be essentially shared when the charge density is taken alone, large scope for important developments appears to be still at hand, when considering the synergy of information from the analysis of several electron distributions or by mixing different experimental techniques, experiments and theories, or by developing new interpretive tools. '*The whole is more than the sum of his parts*' is the underlying idea in a review article by Macchi *et al.* (2015) which appeared recently in **IUCrJ**. That review focused on the possibility 'to extract more information from experimental data, which necessarily means challenging well established models and testing extensions, corrections or even alternative routes' (Macchi *et al.*, 2015). In particular, it recalls that a quite relevant intermediate step has recently been achieved in the long-term quest for a simultaneous refinement of charge, spin and momentum distributions (Gillet *et al.*, 2001; Gillet, 2007 Gillet & Koritsanszky, 2012). Deutsch *et al.* (2012, 2014) could in fact for the first time simultaneously derive both the electron position density $\rho(\mathbf{r})$ and its resolved spin components, $\rho_\alpha(\mathbf{r})$ and $\rho_\beta(\mathbf{r})$ by introducing a spin-split version of the well known Hansen & Coppens (1978) multipolar model to refine the parameters of a multipolar model against X-ray and PND data. Spin-up and spin-down distributions, which for several reasons cannot be accessed from standard refinements (Deutsch *et al.*, 2012, 2014), were found to be in quite good agreement with those obtained from *theoretical* computations. In future, such a model extension should lead to increasingly accurate spin density distributions in crystals, $s(\mathbf{r}) = \rho_\alpha(\mathbf{r}) - \rho_\beta(\mathbf{r})$, which represent most valuable quantities to visualize the magnetic interaction pathways and their signs and therefore a precious tool to understand and design specific magnetic interactions in complex solid-state networks (Gillon *et al.*, 2007; Deutsch *et al.*, 2012, 2014).

Deciphering the mechanisms through which spin information propagates from paramagnetic to non-magnetic centres and the reasons for possible spin polarization effects requires, however, interpretive models, generally based on atomic or molecular orbital pictures, which are inherently unavailable from experiment and represent just a model anyway. A viable and more rigorous alternative is to resort to descriptors directly based on observables, thus applicable also to observables derived from experiment.

Some time ago, Bader & Gatti (1998) introduced the concept of the Source Function (SF), which shows that the electron density $\rho(\mathbf{r})$ at any point in the molecular or crystalline space is caused by *local source* contributions from all other points in the space, $\mathbf{r}'$. The SF enables us to visualize the electron-density distribution in terms of cause–effect relationships (Gatti, 2012), being so profoundly connected to 'one of the main operative notions of chemistry, namely that any local property and chemical behaviour of a system is to some extent always influenced by the remaining parts of the system. Whether such an influence is small or large, it is just quantified through the SF' (Gatti, Saleh & Lo Presti, 2016). Besides investigating whether the SF might also be used to reveal electron delocalization effects in crystals, a recent *Acta Crystallographica Section B* feature article summarizes what the SF descriptor is and shows a number of its applications using electron densities derived from X-ray diffraction data (Gatti, Saleh & Lo Presti, 2016). In another recent paper (Gatti *et al.*, 2015), the SF concept has been extended and applied to the electron spin density (SD). Like the standard SF, the electron spin density Source Function provides quantitative insights into the relative capability of different atoms or groups of atoms in a system to determine the spin density at a given system's locations. It does not only show, within a cause–effect view, how spin information propagates from paramagnetic to non-magnetic centres, but whether also these latter may in turn influence the spin density distribution of the paramagnetic centres themselves. And if so, whether an atom or group of atoms concurs or opposes the paramagnetic centres in determining the spin polarization at a given point and whether it does this in a relevant or negligible measure.

Extension of the SF to the reconstruction of the SD was tested on a water molecule in its triplet state (Gatti *et al.*, 2015) and on alkyl radicals (Gatti, Orlando, Monza & Presti, 2016). Despite the inherent simplicity of these systems, interpretation of the spin density Source Function appears definitely less trivial than the corresponding function for $\rho(\mathbf{r})$. Decomposition of each spin density SF value in a magnetic and in a relaxation (or reaction) term was found not only to ease such an interpretation, providing further very interesting insight (Gatti *et al.*, 2015), but also to be a valid tool to discuss the accuracy of SD distributions. Such an accuracy appears to be a relevant and delicate issue when comparing SD distributions obtained from model wavefunctions of different quality (Boguslawski *et al.*, 2011, 2012; Gatti *et al.*, 2015) or when contrasting experimental and theoretical SD distributions.

As a follow-up to our previous studies, we have applied this novel SF descriptor to the *theoretical* SD distribution of two azido Cu^{II} complexes, using molecular structures taken from their molecular crystals (Aebersold *et al.*, 1998; Aronica *et al.*, 2007). For limits of space, only the results for the end-on complex can be reported in this paper. Those for the end–end complex, along with a comparison between the SF spin density descriptions of the two complexes, will be reported in future work. Our work has several purposes. Firstly, our approach needs to be tested on more complex systems than carried out thus far (Gatti *et al.*, 2015; Gatti, Orlando, Monza & Lo Presti, 2016). Secondly, the kind of information that may be retrieved from a spin density distribution using a descriptor that potentially also applies to experimentally derived spin densities requires further exploration. Indeed, the spin densities of the two compounds we have investigated have in the past also been obtained from standard multipolar model refinements and theoretical computations (Aebersold *et al.*, 1998; Aronica

et al., 2007) and, for one system, also through simultaneous X-ray and PND data refinement (Deutsch *et al.*, 2014). Other purposes of this paper concern an important methodological improvement, related to the problem of easing the choice of the reference points in the SF analysis and to the desire to further assess the capability of our approach to physically analyse and quantify spin density changes as a function of the SD distribution quality.

The paper is organized as follows. §2 reviews the Source Function for the spin density and introduces the concept of partial spin density SF reconstructions due to a given subset of atoms in the system. §3 succinctly describes the two analysed magnetic molecules and their geometrical and magneto-structural features, while §4 reports some computational details. §5 illustrates the SF view of the spin delocalization and polarization mechanisms in the end-on azido Cu^{II} dinuclear complex. §6 outlines the *Conclusions*.

2. The Source Function descriptor

2.1. The Source Function for the electron density

The electron density at any point **r** of a closed quantum system with boundary at infinity is caused by a Local Source (LS), LS(**r**,**r**′), which operates at all other points **r**′ of the system

$$\rho(\mathbf{r}) = \int \mathrm{LS}(\mathbf{r}, \mathbf{r}')\mathrm{d}\mathbf{r}' \qquad (1)$$

and which depends on their electron-density Laplacian values

$$\mathrm{LS}(\mathbf{r}, \mathbf{r}') = -(4\pi \cdot |\mathbf{r} - \mathbf{r}'|)^{-1} \cdot \nabla^2 \rho(\mathbf{r}'). \qquad (2)$$

The factor $(4\pi \cdot |\mathbf{r} - \mathbf{r}'|)^{-1}$ is a Green's function, that is the influence function (Arfken, 1985) characterizing how effective is the cause, $\nabla^2\rho(\mathbf{r}')$, in determining the effect, $\rho(\mathbf{r})$. The whole space integration of the LS may then be conveniently replaced (Bader & Gatti, 1998) by separate integrations over the atomic basins defined through the disjoint and exhaustive space partitioning provided by the surface boundary condition of local null zero-flux of the $\nabla\rho(\mathbf{r})$ vector field, *i.e.* the so-called zero-flux surface recipe of the quantum theory of atoms in molecules, *i.e.* QTAIM (Bader, 1990). Operating in such a way, $\rho(\mathbf{r})$ can be decomposed in terms of the sum of the atomic basin SF contributions

$$\rho(\mathbf{r}) = S(\mathbf{r}, \Omega) + \sum_{\Omega' \neq \Omega} S(\mathbf{r}, \Omega'), \qquad (3)$$

where distinction has been made in the sum between the source from the atomic basin hosting the point where the density is reconstructed, the so-called *reference point rp*, and the cumulative sources from the remaining basins Ω'. Partitioning of space according to the QTAIM recipe ensures a quantum mechanical rigorous association of the sources in equation (3) to the atoms or group of atoms ('functional groups') of the system, though any mutually exclusive or fuzzy space partitioning scheme could in principle also be adopted (Gatti, 2012). Obviously, rigorous association also implies chemical insight since the value of the electron density at a

point and its change upon any perturbation caused by chemical substitution, change of geometry, change of environment, *etc.*, may then be interpreted in terms of how the atoms in a system contribute to determine both of them. By requiring only knowledge of the electron density and of its Laplacian, the SF descriptor is experimentally accessible from X-ray diffraction intensity data through multipole model (MM) refinement (Hansen & Coppens, 1978; Stewart *et al.*, 1975; Volkov *et al.*, 2006; Gatti & Macchi, 2012).

2.2. The Source Function for the spin density

Extension of the SF to the SD case is mathematically straightforward (Gatti *et al.*, 2015). One just needs to replace $\rho(\mathbf{r})$ by $s(\mathbf{r})$, both in the local *cause*, $\nabla^2\rho(\mathbf{r}') \rightarrow \nabla^2 s(\mathbf{r}')$, and in the *effect*, $\rho(\mathbf{r}) \rightarrow s(\mathbf{r})$, while the Green function, $(4\pi|\mathbf{r} - \mathbf{r}'|)^{-1}$, being a purely geometrical (effectiveness) factor, independent from the scalar to be reconstructed, remains unaltered. The symmetry of the $\rho \rightarrow s$ scalar replacement is broken for what concerns the space partitioning in atomic basins. Such a partitioning is, also for the SD, performed using the $\nabla\rho(\mathbf{r})$ zero-flux QTAIM recipe to maintain the rigorous association of atomic source contributions with the quantum atoms or group of atoms of Bader's theory.

The SF decomposition for $s(\mathbf{r})$ will then be expressed as

$$s(\mathbf{r}) = \int_{R^3} \mathrm{LS}_\mathrm{S}(\mathbf{r}, \mathbf{r}')\mathrm{d}\mathbf{r}' = \sum_\Omega \int_\Omega \mathrm{LS}_\mathrm{S}(\mathbf{r}, \mathbf{r}')\mathrm{d}\mathbf{r}' = \sum_\Omega S_\mathrm{s}(\mathbf{r}, \Omega),$$
$$(4)$$

where $S_\mathrm{S}(\mathbf{r},\Omega)$ is the SF contribution from atom Ω to $s(\mathbf{r})$ and the local source for the spin density, LS$_\mathrm{S}$, assumes the form

$$\mathrm{LS}_\mathrm{S}(\mathbf{r}, \mathbf{r}') = -\frac{1}{4\pi}\frac{\nabla^2 s(\mathbf{r}')}{|\mathbf{r} - \mathbf{r}'|} = -\frac{\nabla^2[\rho_\alpha(\mathbf{r}') - \rho_\beta(\mathbf{r}')]}{4\pi|\mathbf{r} - \mathbf{r}'|}$$
$$= \frac{\nabla^2\rho_\beta(\mathbf{r}') - \nabla^2\rho_\alpha(\mathbf{r}')}{4\pi|\mathbf{r} - \mathbf{r}'|}. \qquad (5)$$

Replacement of $\nabla^2\rho(\mathbf{r}')$ by $\nabla^2 s(\mathbf{r}')$ in the local source expression generally leads to quite different atomic sources for the reconstruction of the $\rho(\mathbf{r})$ and $s(\mathbf{r})$ scalars at a given reference point **r** (Gatti *et al.*, 2015). In fact, the two scalar fields were generally found to concentrate [$\nabla^2 u(\mathbf{r}') < 0$, $u = s$ or ρ] or dilute [$\nabla^2 u(\mathbf{r}') > 0$] themselves in a quite distinct manner, implying that the electron density and the SD information transmit themselves with largely different mechanisms throughout a system (Gatti *et al.*, 2015; Gatti, Orlando, Monza & Lo Presti, 2016). The fact that $s(\mathbf{r})$ is given by the difference of the α- and β-electron-density components then yields further peculiarities. Concentration or dilution of both density components is not sufficient to ensure a positive and a negative local source contribution, respectively. What matters is the *relative* concentration or dilution of the two components (Gatti *et al.*, 2015). For instance, when both α- and β-distributions are concentrated, the local source LS$_\mathrm{S}$ will be positive if $|\nabla^2\rho_\alpha(\mathbf{r}')| > |\nabla^2\rho_\beta(\mathbf{r}')|$, while it will be negative if it is the β-density which is more concentrated than the α-density, $(|\nabla^2\rho_\beta(\mathbf{r}')| > |\nabla^2\rho_\alpha(\mathbf{r}')|)$. Conversely, when both distributions are diluted, the local source LS$_\mathrm{S}$ will be positive if $\nabla^2\rho_\beta(\mathbf{r}') >$

Philip Coppens tribute

$\nabla^2 \rho_\alpha(\mathbf{r}')$ and it will be negative if it is the α-density which is more locally diluted, $\nabla^2 \rho_\alpha(\mathbf{r}') > \nabla^2 \rho_\beta(\mathbf{r}')$. The list of all possible cases, including the situations in which one component is concentrated and the other is diluted, is detailed in Table 2 of Gatti *et al.* (2015). A positive local source LS_S [*i.e.* $\nabla^2 s(\mathbf{r}') < 0$] will cause an increase of the α-component of the total electron density, *i.e.* of its α-spin polarization, at a given *rp* $\mathbf{r}$. Such an increase has been named an α *effect*, while a β *effect* (Gatti *et al.*, 2015) is the increase of the β-component at $\mathbf{r}$ caused by a negative local source LS_S [*i.e.* $\nabla^2 s(\mathbf{r}') > 0$]. The α or β nature of the effect is only a function of the source point $\mathbf{r}'$, while its magnitude, besides the spin Laplacian magnitude, is due to the distance from the *rp*.

As anticipated in §1, interpretation of S_S values is not straightforward and it is largely eased and deepened when they are split into a *magnetic* and a *reaction* (or *relaxation*) contribution (Gatti *et al.*, 2015). The former contribution is defined as that due to the distribution of the fully unpaired α-electrons, while the latter is defined as that originating from the distribution of the remaining α and β electrons. The *magnetic* density integrates, over the whole space, to the number of unpaired electrons in the system, while the reaction or relaxation density has an associated SD which integrates to zero over such space, but may, in general, be locally different from zero. It is called *reaction* or *relaxation* density as the $\int \rho_\alpha \equiv \int \rho_\beta$ overall constraint is locally *relaxed* ($\rho_\alpha \neq \rho_\beta$) as a *reaction* to the presence of the distribution of the unpaired electrons. It is worth noting that the magnetic LS_S, though being due only to α-electron density, may have either an α or a β effect, depending on the sign of its Laplacian, while the LS_S due to the reaction density may either counteract or enhance the α or β effect due to the magnetic density. The magnetic density is easily obtained by diagonalizing the first-order density matrix and by selecting, in the evaluation of the density, only those natural orbitals having occupations equal to or very close to one. A thorough discussion and technical details on this mentioned density decomposition is given in Gatti *et al.* (2015), while further technical details relevant to the present work are highlighted in the computational details presented in §4.

2.3. Representations of the Source Function descriptor and selection of the reference points

Atomic SF contributions for the electron density may be analysed as such or more often in terms of Source Function percentage contributions, *S*%

$$S\%(rp, \Omega) = \frac{S(rp, \Omega)}{\rho(rp)} \times 100, \quad (6)$$

which express the relative capability of an atom or group of atoms Ω to determine the electron density at the *rp* (Gatti, 2012). Likewise, Source Function percentages for the SD, $S_S\%$, will be given by

$$S_S\%(rp, \Omega) = \frac{S_S(rp, \Omega)}{s(rp)} \times 100. \quad (7)$$

Regardless of using absolute or percentage SF contributions, the proper choice, if any, of the reference points is one obvious issue to be faced when the SF descriptor is applied. Which guiding criteria should be followed in selecting the *rp*s? Also, once chosen, how can one judge whether the obtained atomic SF patterns are representative or not of a given molecular or crystal region? In other words, why those *rp*s and not any other?

When dealing with the investigation of chemical bond features, it looks reasonable to take the electron-density bond critical points (BCPs; Bader, 1990) as the most representative and least biased choices for *rp*s associated with a bonding interaction (Gatti *et al.*, 2003; Gatti, 2012). There may also be the case where significant electron sharing exists between two atoms despite the fact that they are not connected by a bond path (Pendás *et al.*, 2007; Farrugia *et al.*, 2006; Gatti & Lasi, 2007; Ponec & Gatti, 2009; Gatti, 2013). In this event, the evaluation of SF contributions at the internuclear axis mid-point and along the whole axis was found to be appropriate (Farrugia *et al.*, 2006; Gatti & Lasi, 2007; Gatti, 2012). However, the most suited choice of *rp*s becomes less evident when considering the electron spin density SF reconstructions. For instance, it has been found that the SD is often minimized at BCPs, because at these positions, particularly for covalent bonds, electron pairing is maximized and the magnetic density only plays a minor role here (Gatti *et al.*, 2015; Gatti, Orlando, Monza & Lo Presti, 2016). Representative points for such density, which largely determines the SD in the high α-polarization density regions, have been taken at the critical points of the electron-density Laplacian distribution associated with unpaired electrons and, for the sake of comparison, also at the $(3, -3) -\nabla^2 \rho$ critical points associated with lone pair electrons (Gatti *et al.*, 2015). However, such choices are somewhat arbitrary and possibly biased. An obvious solution, which is presented here for the first time, is to calculate the SF contributions from a given subset of the atoms in the system at an *N*-dimensional grid of *rp*s. In this way, cube ($N = 3$), surface ($N = 2$), line ($N = 1$) or point ($N = 0$) electron or electron spin *partially* reconstructed densities are obtained

$$\rho\{\Omega, subset\}(\mathbf{r}) = \sum_{\Omega, subset} \int LS(\mathbf{r}, \mathbf{r}')d\mathbf{r}' = \sum_{\Omega, subset} S(\mathbf{r}, \Omega) \quad (8)$$

$$s\{\Omega, subset\}(\mathbf{r}) = \sum_{\Omega, subset} \int LS_s(\mathbf{r}, \mathbf{r}')d\mathbf{r}' = \sum_{\Omega, subset} S_s(\mathbf{r}, \Omega). \quad (9)$$

When the subset includes all the atoms of the system, these reconstructed densities are no longer *partial*. Their deviations from the corresponding densities are usually negligible and provide just a measure of the numerical quality of the reconstruction through the SF descriptor. When, instead, only an atom or a subset of the atoms of the system is considered in equation (8) or (9), the role this atom or group of atoms has in determining either the electron or the SD in a given region of space becomes manifest. Note that there is a profound difference between the SF partially reconstructed densities and those partial density representations one may obtain using

a subset of pseudoatom densities in the multipolar model approaches (Volkov *et al.*, 2006) or using only the contributions from the basis functions of a subset of atoms in a *theoretical* computation. The SF partially reconstructed densities yield a *cause–effect* picture of atomic contributions in determining a given density and in this respect are fully unbiased. The information they provide is only a function of the total density they partially reconstruct. The *standard* partial densities, instead, refer to actual density contributions from pseudoatom monopolar density functions or from atomic basis set functions and depend, not only on the total density, but also on the specific multipole model or atomic basis set adopted. At the limit, if a complete basis set centred on a point other than a nuclear position were used in a *theoretical* computation, the resulting electron or spin density would be the best which could be obtained within the chosen wavefunction expression, yet all partially reconstructed densities would be equal to zero everywhere.

Partially reconstructed densities may be portrayed as such or as percentage reconstructed densities. When $N = 0$, percentage sources are typically shown in a ball-and-stick representation for all atoms in a system (or at least for those atoms yielding significant sources). Each atom is assigned a volume proportional to its SF percentage contribution and such a representation pictorially illustrates whether the reconstruction of the density at the rp is made in terms of very localized or in terms of partially or totally delocalized sources. On the other hand, when compared with the total density, the two-dimensional contour maps of the partially reconstructed densities give a very clear indication of how an atom or a subset of atoms contribute to determine the electron or the SD in the selected plane. These maps thus depict whether in a given molecular region such a contribution is important, modest or negligible and whether it remains almost stable or significantly varies within the region. These maps may therefore be quite useful for a proper selection of the reference point for an $N = 0$ representation and for a full understanding and relevance assessment of such a representation.

As a summarizing example, Fig. 1 illustrates a number of representations of the electron spin density SF contributions (Gatti *et al.*, 2015) in the triplet $^3B_1$ H_2O system (Herzberg, 1966) computed at the CASSCF(8,8) level and using a 6-311++G(2d,2p) basis set. In the first row of the figure, a ball-and-stick $N = 0$ representation of the atomic SF percentage contributions at the O—H BCP ($s = -0.008$ a.u.) is shown for the total SD and for its magnetic and relaxation components. Green (red) balls denote an α (β) effect on the density at this rp, while SF percentage contributions are taken as positive or negative, whether the sources have the same or the opposite sign of the density value at the rp. It is clear that in the molecular plane there is a spin polarization mechanism, since the H atoms determine positive SD contributions at the BCP, and hence have an α effect, while the O atom behaves in the opposite manner and its dominant β effect leads to a negative SD at the BCP (Gatti *et al.*, 2015). Surprisingly, H and H′ atoms yield very similar sources (-29.1 and -25.5%, respectively), despite the rp relating only O and H directly,

suggesting that some compensating mechanism is operative here. The relaxation term, which yields a β effect for all atoms, neatly differentiates the effects of H and H′, similar to what is found when the electron density is reconstructed (Gatti *et al.*, 2015). It is the dominant and, as far as the H atoms are concerned, opposing magnetic term that eventually leads to similar total sources from the two H atoms. Due to spin delocalization and polarization effects, the magnetic source from H is only four times larger than that of H′ (-117.8 *versus* -31.4%), while the corresponding relaxation sources, which are related to a through-bond covalent mechanism and are therefore more local in nature, differ by a factor almost four
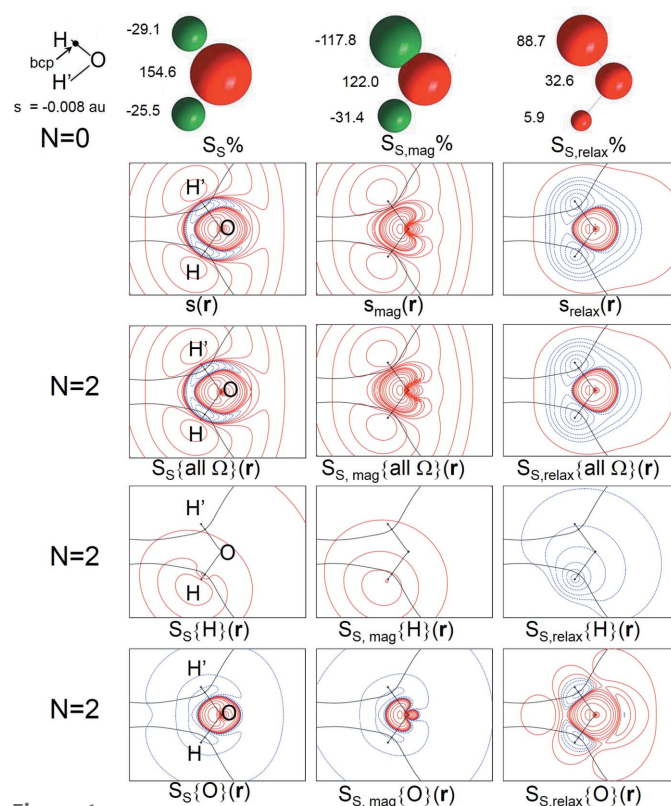

Figure 1
N-dimensional representations of the electron spin density (SD) Source Function contributions for triplet $^3B_1$ H_2O at the CASSCF(8,8) level and using a 6-311++G(2d,2p) basis set. Source Function contributions, electron SD, and total and SF partially reconstructed densities are shown for the SD and for its magnetic and relaxation components. First row: SF percentage contributions for a reference point taken at the O—H bond critical point. Green (red) atomic balls denote an α (β) effect on the density at the reference point. SF percentage contributions are positive or negative whether they concur or oppose to reconstruct the density value at the reference point. Second row panels: two-dimensional contour plots of the total SD and of its components in the molecular plane [red are positive and dotted blue are negative contour values; contour maps are drawn at an interval of $\pm(2,4,8) \times 10^n$, $-4 \leq n \leq 0$ atomic units (a.u.)]. Full black lines mark boundaries of atomic basins. The same conventions and isovalue contour lines occur in all maps of the figure. Third row panels: SF reconstructed densities in the molecular plane, using the sources of all atoms in the molecule. Fourth row panels: as in the third row, but excluding the H′ and O sources. Fifth row panels: as in the third row, but excluding the H and H′ sources. The first row illustrates an $N = 0$ (zero-dimensional) SF% representation, while the panels in the other rows are $N = 2$ (two-dimensional) SF representations. [SF AND SF% OK]

times as large. The quite different decay law with distance from the *rp* of the (here opposing) magnetic and relaxation H-atoms sources is the ultimate reason for their similar total sources at the O—H BCP. The second row panels in Fig. 1 display contour plots for the SD and its magnetic and relaxation components in the molecular plane. SF reconstructions of such densities using all the atoms of the molecule (third row panels, Fig. 1) lead to essentially identical plots, indicating that the SF numerical reconstruction is almost perfect in this case. The negative SD regions are due to the relaxation spin density, since the magnetic SD of all atoms is positive everywhere, as it must be by definition. The spin polarization mechanism is clearly evident along the bond paths and in significant parts of the O-atom basin. More insight is obtained when all the atom reconstructions are compared against the $N = 2$ SF *partial* SD reconstructions. Those excluding H′ and O atoms are shown in the fourth row panels and those excluding H and H′ atoms in the fifth row panels. From an inspection of the left panels it is evident that only the O atom is responsible for the regions of negative SD in the molecular plane (β effect). In such a plane, its α effect is limited to a region close to its nucleus, while each H atom yields only an α effect everywhere. For H atoms, the magnetic density everywhere is positive and dominating over the negative relaxation density. The magnetic density due to the H atoms also prevails over the negative magnetic density brought in by the oxygen in some regions of the molecular plane, thus ensuring the magnetic density to be positive everywhere, as required. The O atom has a region of reinforcing positive magnetic and relaxation SDs around the nucleus, but also displays regions where these densities are both negative (along the bond path and close to the BCPs and the hydrogen nuclei) or, instead, oppose each other, as in the case of the H atoms.

3. Structural and magnetostructural aspects of the investigated azido-bridged dicopper complexes

Azido-bridged polymetallic species have been largely synthesized and studied since the 1980s for their structural diversity and their interesting and challenging magneto-structural relationships (Aronica *et al.*, 2007, and references therein). The azido group, *i.e.* N_3^-, is a non-innocent ligand and one of the most interesting magnetic couplers in molecular magnetism (Aebersold *et al.*, 1998, and references therein). We have performed an SF analysis of the SD in two azido-bridged dicopper molecular complexes, namely [$Cu_2(t\text{-}Bupy)_4(N_3)_2$](ClO$_4$)$_2$ [t-Bupy = p-$tert$-butylpyridine] and $Cu_2L_2(N_3)_2$ (L = 7-dimethylamino-1,1,1-trifluoro-4-methyl-5-azahept-3-en-2-onato), whose geometries have been taken from their molecular crystal structures, using the 18 (Aebersold *et al.*, 1998) and 150 K (Aronica *et al.*, 2007) X-ray geometries, respectively. The Cu^{II} cations in the complexes are coupled through two azido bridges; in the former complex, the azido groups are symmetrically linked to the Cu^{II} cations through one terminal N atom (μ-1,1) (end-on, EO coordination mode), resulting in two short equivalent N—Cu bonds. In the second complex, two terminal N atoms (μ-1,3) (end-to-end, EE coordination mode) coordinate asymmetrically, *i.e.* with one short and one long N—Cu bond, the two metal centres. Fig. 2 summarizes the relevant structural data. Both complexes are centrosymmetric, with Cu′···Cu distances as large as $\simeq 3$ (EO) and 5 Å (EE), and ions ferromagnetically coupled to a different extent [J(EO) = 300 cm^{-1} and J(EE) = 17 cm^{-1}] (Aebersold *et al.*, 1998; Aronica *et al.*, 2007). Symmetrically linked azido groups lead to Cu′···Cu intramolecular magnetic coupling which varies from strongly ferromagnetic to strongly antiferromagnetic, depending on the coordination mode (Aebersold *et al.*, 1998). The EO complexes exhibit a triplet ground state (ferromagnetic, FM, coupling) because of the quasi-orthogonality of the Cu^{II} magnetic orbitals for the range of observed values of the Cu′—N—Cu bridging angle, while the EE complexes always show a singlet spin state (antiferromagnetic, AF, coupling) due to the strong overlap between these orbitals (Aronica *et al.*, 2007). For asymmetrically bridged complexes, the picture is less definite (Aronica *et al.*, 2007). EO compounds may show AF coupling, while EE complexes may exhibit FM coupling, as in the present case, or, more commonly, an AF coupling. Regardless of the AF or FM nature, coupling in the EE asymmetric systems is, however,
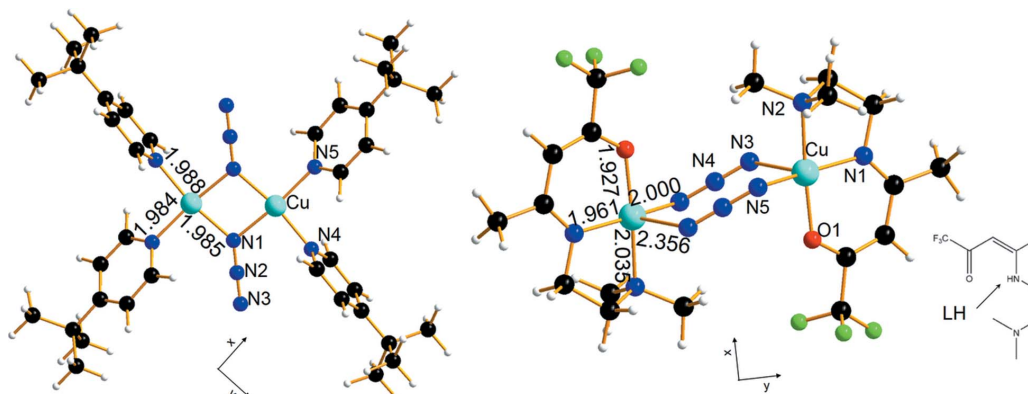

Figure 2
Molecular structure, atomic labelling and geometrical data for the FM end-on (left) and the FM end–end (right) centrosymmetric azido-bridged dicopper molecular complexes. Bond distances are in Å. Black, white and green balls denote C, H and F atoms, respectively.

Table 1
Net charges (q), spin populations (SP) and atomic spin density Laplacian (ASDL) for selected atoms or atom groups Ω in the end-on FM azido Cu^{II} dinuclear complex.

QTAIM partitioning: $q(\Omega)$ and SP(Ω); Mulliken's partitioning: SP$_M$ (Ω); polarized neutron diffraction estimate: SP$_{PND}$(Ω); ASDL = $\int_\Omega \nabla^2 s$ d**r**.

Ω	$q(\Omega)$†	SP(Ω)†	SP$_M$(Ω)†	SP$_{PND}$(Ω)‡	SP$_M$(Ω)‡§ (Abersold simplified structural model)	ASDL†
Cu	1.433 (1.095)	0.899 (0.619)	0.919 (0.628)	0.783 (7)	0.425	−0.206 (−0.085)
N1	−0.642 (−0.488)	0.032 (0.095)	0.024 (0.089)	0.069 (6)	0.167	0.098 (0.036)
N2	−0.216 (−0.138)	−0.009 (0.005)	−0.013 (−0.007)	−0.016 (6)	−0.005	0.025 (0.064)
N3	0.126 (+0.039)	0.028 (0.088)	0.030 (0.100)	0.057 (7)	0.122	−0.018 (−0.047)
Azide	−0.733 (−0.587)	0.051 (0.188)	0.041 (0.182)	0.110 (19)	0.284	0.105 (0.053)
N4	−1.464 (−1.056)	0.022 (0.087)	0.018 (0.088)	0.067 (8)	0.129	0.048 (0.001)
N5	−1.496 (−1.083)	0.022 (0.079)	0.018 (0.080)	0.049 (7)	0.120	0.048 (0.002)
$\sum C_{py}$(N4)¶	1.224 (0.877)	0.002 (0.008)	0.002 (0.004)	−0.037 (46)	0.009	–
$\sum C_{py}$(N5)¶	1.264 (0.914)	0.002 (0.008)	0.002 (0.004)	0.005 (52)	0.008	–

† Data from the CASSCF(6,6) wavefunction (in parentheses those from UB3LYP). ‡ Data from Table 5 of Aebersold *et al.* (1998). Estimated standard deviations in parentheses. § A simplified [Cu$_2$(py)$_4$(N$_3$)$_2$]$^{2+}$ (py = pyridine) system was used in the DFT calculations reported by Aebersold *et al.* (1998). ¶ $\sum C_{py}$(N4) and $\sum C_{py}$(N5) refer to the sum of the properties of the C atoms in the pyridine rings having N4 or N5 has their N atom.

always very low. In fact, in a square-pyramidal geometry coordination of Cu^{II} (Fig. 2), one terminal azido N atom points to the $d_{x^2-y^2}$ magnetic orbital of one Cu^{II} cation, forming the short Cu—N bond, while the other points to the d_{z^2} orbital of the second Cu^{II} cation, forming the long Cu′—N bond and implying a weak or negligible interaction. As stated before, only results for the EO symmetric complex will be reported in the following. Due to space constraints, the discussion on the relationships between the different structural arrangements around the Cu^{II} cation, the strong or weak Cu′···Cu FM couplings and the different SF spin density portraits in the EO and EE complexes will be reported in future work.

4. Computational details

Theoretical SD computations for the triplet ground states of the EO azido-bridged dicopper molecular complex were performed *in vacuo* and at its crystalline geometry by means of the *GAUSSIAN*09 program package (Frisch *et al.*, 2009). Both the double positively charged and the neutral complexes were calculated, but results are discussed only for the former, as their spin distributions were found to be almost indistinguishable. Complete active space self-consistent field (CASSCF), UB3LYP (unrestricted B3LYP) and UHF (unrestricted Hartree–Fock) levels of theory were adopted for both complexes, employing the pob-TZVP basis set (Peintinger *et al.*, 2013) for all methods. The reported UB3LYP results refer to spin-contamination annihilated wavefunctions. Spin contamination by states of higher multiplicity than the triplet state was minor [$\langle S^2 \rangle$ = 2.0109] and almost zero after the annihilation procedure [$\langle S^2 \rangle$ = 2.0001]. CASSCF computations included six electrons in the active space composed of six orbitals [CASSCF(6,6)], *i.e.* four occupied and two virtuals in the initial guess determinant. The starting orbital guess for the CASSCF computation was taken from the UB3LYP spin-contamination annihilated natural orbitals. The active orbitals were chosen in an analogous manner to those adopted in the model by Aebersold *et al.* (1998), selecting both *gerade* and

ungerade symmetries. The UHF method gave serious self-consistent field convergence problems and high spin contamination of the resulting wavefunction, even after spin-contamination annihilation. UHF results are therefore not discussed in the paper, although we checked that the CASSCF converged spin density was practically the same, whether the natural orbitals from the UHF or from the UB3LYP calculations were used as a starting guess. The Slater determinant expansion of the CASSCF(6,6) wavefunction includes 225 configurations of the correct symmetry and spin multiplicity. The magnetic density of the UB3LYP and CASSCF wavefunctions was calculated from their natural orbitals obtained through the 'pop = NO' option and by selecting only those with occupation numbers equal to one or marginally different from one (highest deviation from one being 0.00029). Spin densities for the various wavefunctions were obtained following the same sequence of intermediate steps detailed in the supplementary information of Gatti *et al.* (2015).

Topological analysis of the ρ and $\nabla^2 \rho$ scalar fields was performed through a modified version of the *AIMPAC* program package (Biegler-König *et al.*, 1982). Other home-developed codes have been used to evaluate: (*a*) atomic Source Function contributions to the electron density, the spin density and its magnetic and relaxation components at selected reference points or at the points of an N (N = 1–3) dimensional grid (SPINSF2016 code); (*b*) spin density and spin density Laplacian, also resolved in their α and β contributions at given positions (EXTREMESPIN code); (*c*) contour two-dimensional maps of the spin density, of the spin density Laplacian and of their magnetic and relaxation densities counterparts; (*d*) contour two-dimensional maps of the SF reconstructed partial spin densities and their magnetic and relaxation density counterparts (PLOTDEN2016 code). SPINSF2016 and EXTREMESPIN codes are heavily modified versions of the original PROAIMV and EXTREME codes of the *AIMPAC* program package, while PLOTDEN2016 is an updated and unpublished version of the PLOTDEN2013 code (also unpublished, but with a brief description in the

supporting information of Gatti *et al.*, 2015). The *DIAMOND* code (Putz & Brandenburg, 1997–2012) was employed to draw all the ball-and-stick pictures.

5. SF view of the spin delocalization and polarization mechanisms in the end-on azido copper(II) dinuclear complex

5.1. Spin density populations

QTAIM theoretical net charges $q(\Omega)$ and spin populations $SP(\Omega)$ for selected atoms or group of atoms for this complex are listed in Table 1. Hereinafter, in the text, tables and figures the term Cu^{II} *cation(s)* is replaced by Cu^{II} *atom(s)* whenever properties of the QTAIM basin(s) or of those derived from Mulliken's partitioning are referred to. In Table 1, QTAIM results are compared with those obtained by Aebersold *et al.* (1998) from PND data refinement and DFT calculations. Since these latter used a standard Mulliken's population-analysis approach, Mulliken's atomic spin populations, $SP_M(\Omega)$, are also reported from our calculations, for the sake of comparison. The theoretical data shown in Table 1 demonstrate a large dependency on the method (CASSCF or DFT), DFT functional and basis set adopted. The total spin population of 2 *e* is predicted to be 90% resident on the Cu atoms by the CASSCF(6,6) approach, while this value is reduced to 63 and 43% by our and the Aebersold *et al.* (1998) DFT Mulliken estimates, respectively. Aebersold *et al.* (1998) use a TZVP-type basis set, different from ours, but of similar quality, while for spin density calculations they adopt a local rather than a hybrid DFT functional. The discrepancy between the two DFT results should thus be ascribed mainly to the quite different kind of DFT functional and, possibly, also to the use of a simplified model structure (*tert*-butyl groups replaced by H atoms) in the Aebersold *et al.* (1998) calculations. The PND estimate, 78% of spin population resident on the Cu atoms, is intermediate between the CASSCF(6,6) and our DFT result, but closer to the former. Note that the much higher net positive charge of the Cu atom predicted by CASSCF(6,6) ($q = 1.433$ *e*), relative to our DFT estimate ($q = 1.092$ *e*), may affect the spin population also. QTAIM and Mulliken's spin populations are close to each other, when using the same wavefunction method (compare the data in columns 3 and 4 of Table 1). Yet, their small differences are capable of changing the sign of the population from positive to negative or *vice versa*, when the populations are small in magnitude (*e.g.* for the central atom of the azido ligand, *i.e.* N2).

Overall, the CASSCF(6,6) method predicts that *ca* 5.1% of the spin population is delocalized over the azido ligands and the remaining 4.4% over the pyridine N atoms, while other atoms in the system bear almost negligible spin populations. Spin delocalization is about *four times as large* at the UB3LYP level on both the azido and the pyridine N atoms, while it is predicted to be about 2.5 times as large by PND. Exchange–correlation functionals, including the hybrid ones, like UB3LYP, are indeed known to be unable to reproduce the CASSCF spin densities accurately (Boguslawski *et al.*, 2011).

Instead, CASSCF wavefunctions, with an adequate active space, are definitely much closer to the spin densities obtained through density-matrix renormalization group (DMRG) methods, which may be considered as an (almost) exact reference for such densities (Boguslawski *et al.*, 2012). Besides, SD distributions are known to also depend on the approximate exchange−correlation density functional if transition metal complexes containing non-innocent ligands are considered (Conradie & Ghosh, 2007; Boguslawski *et al.*, 2011). In our work on both the EO and the EE complexes, the UB3LYP method was selected for the sake of comparison with previous studies on the EE complex (Aronica *et al.*, 2007; Deutsch *et al.*, 2014) and for the need to use the same DFT functional to properly compare the spin densities in the EO and EE complexes.

Assuming, therefore, CASSCF(6,6) as the best theoretical estimated SD among those discussed here for the EO complex, it is concluded that both UB3LYP and the local functional adopted by Aebersold *et al.* (1998) exaggerate the extent of spin delocalization in the complex. Yet these methods are able to predict almost correctly the *relative* weight of spin delocalization among the ligands of the system. In particular, there is a general consensus for N2 having the smallest spin population in the azido group. The smaller positive charge of Cu in the UB3LYP calculation may also be related to the excessive spin delocalization to ligands, which causes, as a reaction mechanism, the formation of small negative SD regions between the Cu and its bonded N atoms. Such spin polarization mechanisms should favour partially covalent rather than pure dative Cu−N bonding, leading to a decreased positive charge on Cu, relative to CASSCF(6,6).

The CASSCF(6,6) estimates are closer to the experimental PND results, but still far from them. Shortcomings of the PND data refinement might explain the observed discrepancies, in particular, the higher spin delocalization found by PND. Indeed, only a very small data set of 152 magnetic structure factors could be considered by Aebersold *et al.* (1998) in the refinement and an MM including either only one spherical or only one angular Slater atomic function on each atom could be adopted. Convergence of CASSCF estimates with increasing computational quality should, however, also be examined. Increasing the size of the active space from CASSCF(6,6) to CASSCF(6,8) and CASSCF(6,10) models does not influence significantly either the energy or the atomic SD populations, despite the number of included configurations being increased from 225 to 1960 and 9450, respectively. For instance, the energy is lowered by 0.00012 [CASSCF(6,8)] and 0.00017 a.u. [CASSCF(6,10)], while the SD populations of the Cu atom, of the azido group and of the pyridine N atoms all remain unaltered within 0.0005 *e* in both model calculations. At the CASSCF(6,10) level, small changes are found for the *individual* SD populations in the azido group, the largest changes being −0.008 *e* for N3 and 0.006 *e* for the N2 atoms. On the other hand, increasing the number of correlated electrons is instead a far more delicate issue. To ensure a selection compatible with the symmetry of the system, this number needs to be raised from 6 to at least 14 (two π electrons for

each pyridine unit), leading to too demanding, if not impossible, computations if one wishes to retain a basis set size of sufficient quality for treating electron correlation adequately. CASSCF models with an intermediate number of active electrons (8 and 10) have nonetheless been considered. The CASSCF(10,10) model leads to small asymmetries in the SD populations, with an enhanced SD population for the pyridine N (only for those two pyridine units having their electrons correlated) and a slow decrease of the Cu SD population (0.85 e). Despite being physically incorrect, these CASSCF calculations with an 'intermediate' number of active electrons suggest that increasing their number to 14 e could lead to an even closer agreement between CASSCF and PND atomic SD populations.

Weighing up the rapid convergence of the CASSCF tests with a fixed number of electrons and increasing orbital active space, and, conversely, the restraints on the number of active electrons, reasonably affordable in CASSCF computations, we have decided to limit our analysis of CASSCF results only to those obtained with the CASSCF(6,6) model.

5.2. Spin, magnetic and relaxation density maps and their atomic Source Function origin

Spin density maps for the CASSCF(6,6) and UB3LYP calculations, in the least-squares plane of the four ligand N atoms around each Cu^{II}, are shown in Fig. 3, along with their magnetic and relaxation densities components.

Comparison of the corresponding maps between the two theoretical methods highlights the much greater spin delocalization on the atoms of the ligands occurring at the UB3LYP relative to the CASSCF(6,6) level and shows that both the magnetic and relaxation components concur to such an enhancement. Both methods agree that there exists an important spin polarization mechanism in the azido group, with a significantly large region of negative SD around the N2 atom, reflected in its almost negligible spin population. The negative region around N2 is obviously due to the SD relaxation component (compare the right and left panels in Fig. 3). However, UB3LYP and CASSCF(6,6) predict quite different portraits for it. The s_{relax} negative region around Cu^{II} atoms seems an artefact of the UB3LYP method and it is in turn responsible for the SD negative region close to the boundaries of the Cu basins evident in the UB3LYP map (Fig. 3, lower row, left panel). Such a region is totally absent in the CASSCF(6,6) SD map (Fig. 3, upper row, left panel), except for a tiny area between Cu^{II}

and the bridging N1 atom. The UB3LYP and CASSCF(6,6) relaxation SDs also differ with regard to the extent of spin polarization around N2 and the presence in the UB3LYP map of an extended positive region around N1, which is totally lacking in the CASSCF(6,6) map. Besides that, the CASSCF(6,6) relaxation SD around the Cu^{II} cations displays the same $d_{x^2-y^2}$ angular shape as the SD (refer to Fig. 2 for axes orientation), whereas a much more rounded, almost spherical, shape is visible in the UB3LYP relaxation SD map.

Table 1 also lists the value of the atomic SD Laplacian (ASDL), $\int_\Omega \nabla^2 s \, d\mathbf{r}$, while Fig. 4 shows the $\nabla^2 s$ scalar field isolines in the same plane of Fig. 3. At variance with the atomic electron-density Laplacian, $\int_\Omega \nabla^2 \rho \, d\mathbf{r}$, ASDL usually differs from zero because the atomic boundary surface is defined in terms of the local zero flux of $\nabla \rho$ and not of that of ∇s. ASDL values provide a measure of whether, on average, a QTAIM atomic basin has a prevailing α (ASDL < 0) or β (ASDL > 0) effect, though its specific effect on a given rp will depend on how the Green's term locally weights the integrand $\nabla^2 s$ in the SF_S expression. The Cu atom, which holds most of the unpaired density, has a negative and the largest (in magnitude) ASDL, indicating a prevailing α effect, while all N atoms of the ligands, except the terminal N atoms of the azido groups, have a positive ASDL and a prevailing β effect. The features of $\nabla^2 s$ maps (Fig. 4) provide further details. The capability of the Cu atom to produce an α effect is due to the dominance of the dotted blue regions ($\nabla^2 s < 0$), which are very localized, directed towards the ligands and characterized by high $|\nabla^2 s|$ values. The negative $\nabla^2 s$ region around the copper has the shape of a squeezed Cu^{II} $d_{x^2-y^2}$ atomic orbital surrounded by a large positive $\nabla^2 s$ region where the copper yields a counteracting β effect. However, on average, the α effect prevails, as indicated by the Cu negative ASDL value.
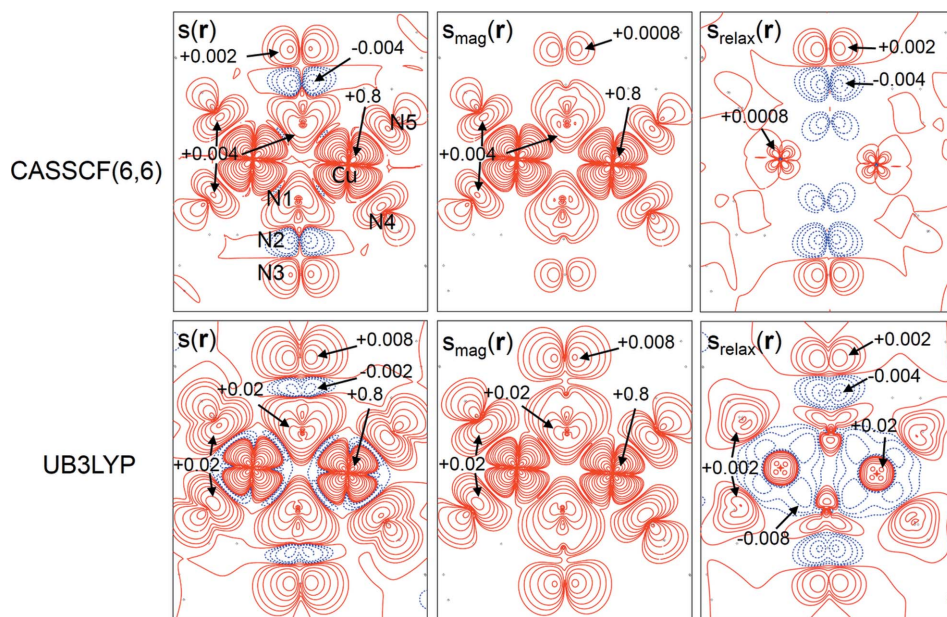

Figure 3
End-on FM complex: CASSCF(6,6) and UB3LYP contour plots of the spin density (left panel) and of its magnetic (central panel) and relaxation (right panel) components in the least-squares plane of the four ligand N atoms around each Cu^{II}. The same colour codes and isovalue contours apply as in Fig. 1.
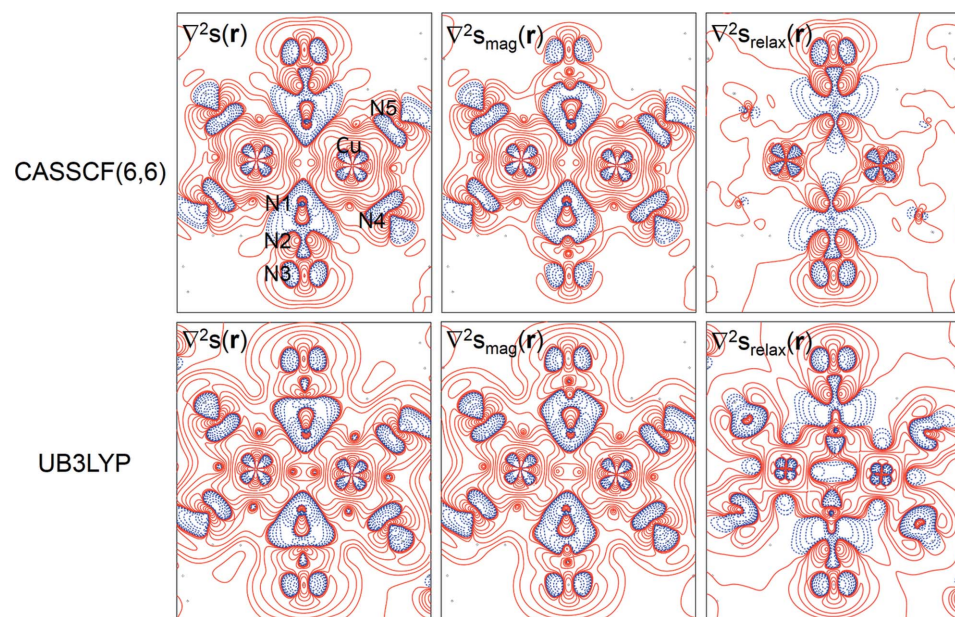
Figure 4
End-on FM complex: CASSCF(6,6) and UB3LYP contour plots of the spin density Laplacian (left panel) and of its magnetic (central panel) and relaxation (right panel) components in the least-squares plane of the four ligand N atoms around each Cu^{II}. The same colour codes and isovalue contours apply as in Fig. 1.

average, over the β effect regions close to their nuclei. This holds particularly true at the CASSCF(6,6) level. The α effect regions of the N atom linked to Cu^{II} are those able to determine delocalization of the unpaired electron density. The central atom of the azido ligand has also a prevailing β effect, whereas the terminal N atom behaves in an opposite manner as a result of its π-like and dominating α effect regions. Spin polarization in the azido ligands is also evident from the opposing average spin density source effects produced by the terminal and the other two N atoms of the group, with these latter prevailing when the whole azido group is considered (Table 1, ASDL > 0 for the azido group). UB3LYP and CASSCF(6,6) spin density Laplacian maps differ for their relaxation components, which
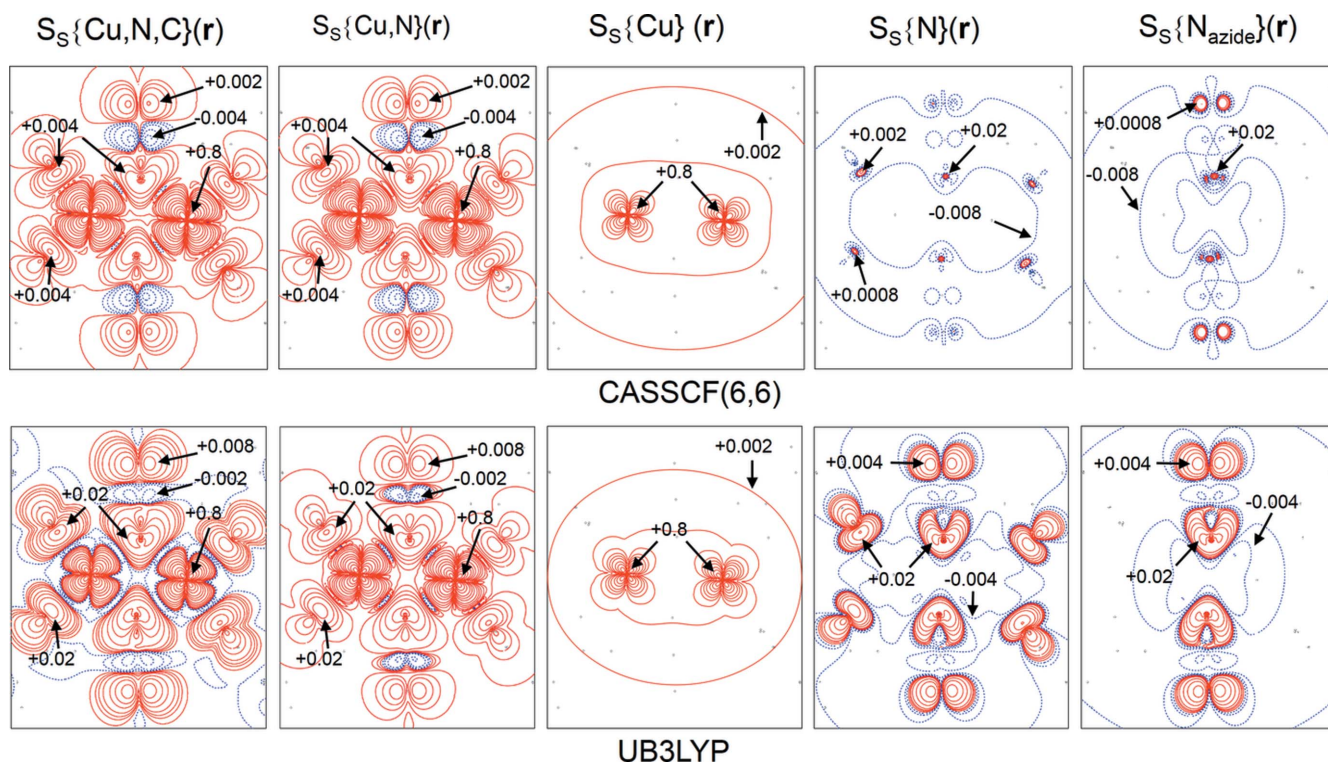
Fig. 4 also shows that the bridging and pyridine N atoms have negative $\nabla^2 s$, α effect regions, pointing towards copper and wider than those of Cu atoms, but unable to prevail, on are significantly different in shape and local scalar magnitude, while the magnetic components are, at least as for their shape, closer to each other.

Figure 5
End-on FM complex: CASSCF(6,6) (up) and UB3LYP (down) contour plots of the SF reconstructed partial spin densities, $S_s(\Omega_{subset})(\mathbf{r})$ in the least-squares plane of the four ligand N atoms around each Cu^{II}. The corresponding magnetic and relaxation components are shown in Figs. S1–S2. In the maps, {Cu, N, C} denotes the subset of the atoms of the system including the two Cu atoms, all N atoms and the C atoms of the pyridine rings. Similar labelling is used for the group of atoms included in the other listed subsets, with N_{azido} denoting an N atom of the azido groups only. The same colour codes and isovalue contours apply as in Fig. 1.

SF reconstructed partial densities (Fig. 5, Figs. S1–S2 of the supporting information) provide a cause–effect view of the SD and of its components. Group subsets {Cu, N, C}, {Cu, N}, {N}, {N$_{azido}$} are considered, where {Cu}, {N} and {C} denote the subsets including the two Cu atoms, all N atoms and all C pyridine rings atoms, respectively, while {N$_{azido}$} denotes only the N atoms of the azido ligands. Figs. S1–S2 compare these reconstructed partial spin densities with their corresponding magnetic and relaxation density components, while Fig. 6 reports such a comparison also for the subsets including the bridging, {N1,N1′}, the central, {N2,N2′}, and the terminal, {N3,N3′}, atoms of the azido groups.

Including all atoms in the atomic subset, except the pyridine H and those of the *tert*-butyl groups, leads to SF{Cu, N, C} reconstructed partial density maps almost indistinguishable from their *primitive* maps, indicating that the contributions from the excluded atoms are negligible (*cf.* Figs. and 5). The only noticeable differences concern the peripheral regions of the map and this consideration holds true both for the SD and for its magnetic and relaxation components (Fig. S1). When the pyridine C atoms are also excluded from the reconstruction, important differences begin to emerge, essentially at the UB3LYP level. For instance, the negative SD region surrounding the Cu atoms and close to their atomic boundaries appears to be mostly due to the effect of the pyridine C

atoms (compare the first and second lower panels in Fig. 5 and the second row *versus* the fourth row panels in Fig. S1). The negative density regions in the relaxation SD map contract and so do the regions of very high positive density around the Cu^{II} cations in the magnetic density map (Fig. S1, second and fourth row panels). The fact that only the UB3LYP densities appear to be significantly affected by the exclusion of the SF contributions of relatively remote atoms in the molecular regions mapped in Figs. 5 and S1 further confirms that the UB3LYP likely exaggerates spin delocalization mechanisms. Interestingly, this appears true not only in the direction from the paramagnetic atoms to the ligands, but also the other way round. This reversed direction *may be only appreciated through the SF analysis and within a cause–effect context*. The third panel in the first (CASSCF) and second (UB3LYP) rows of Fig. 5 illustrates the SD source from the Cu atoms. As expected, it is the most relevant source and the one that imparts the $d_{x^2-y^2}$ symmetry to the total SD. It is always positive (in this plane) and it is dominated by the magnetic component (see Fig. S2). The Cu + Cu′ SD source is larger in magnitude at the CASSCF level (compare the UB3LYP and CASSCF contour level values in Fig. 5) since, differently from CASSCF, the UB3LYP model predicts, in the relaxation SD map, large regions of opposing negative SD sources besides those of positive sign close to the Cu nuclei. The fourth and
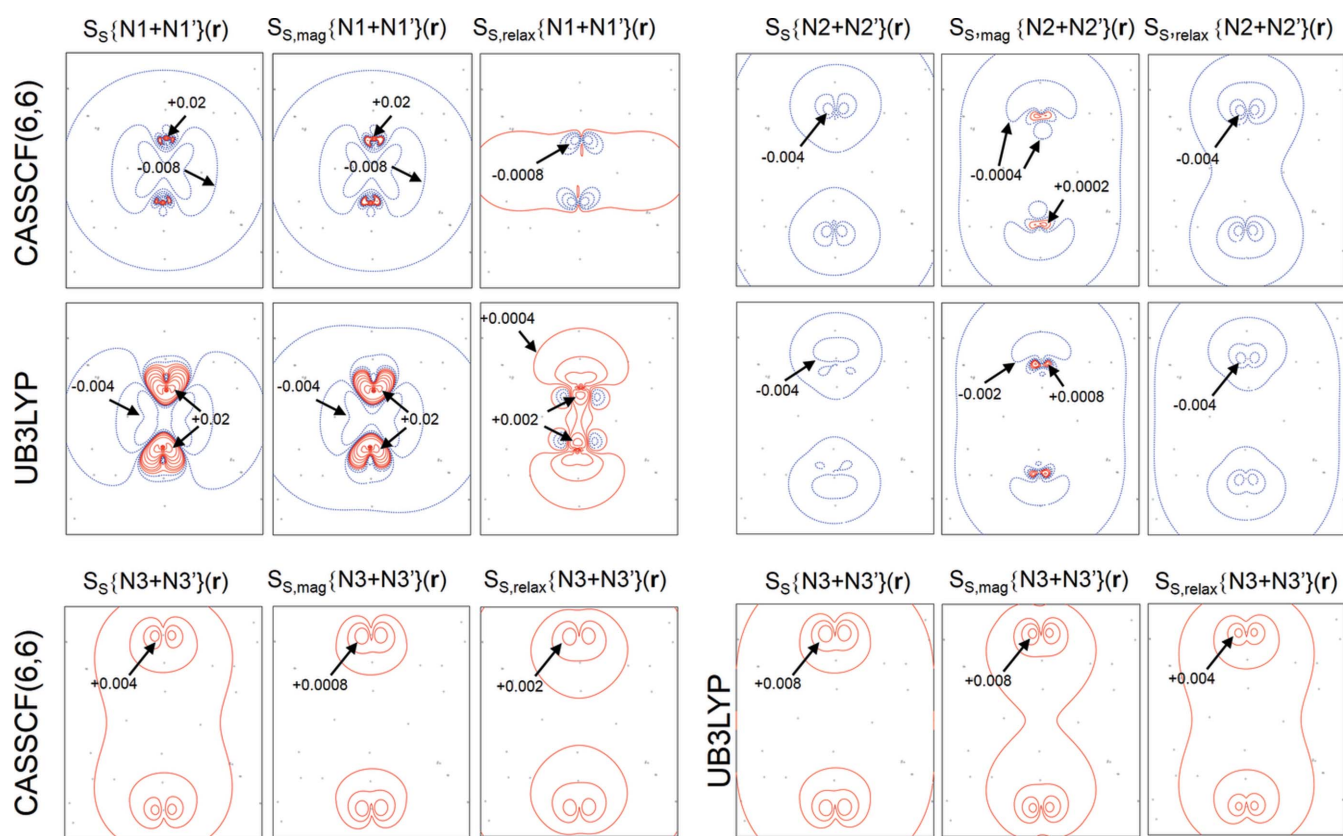

Figure 6
End-on FM complex: CASSCF(6,6) and UB3LYP contour plots of the partially SF reconstructed spin densities, $S_s(\Omega_{subset})(\mathbf{r})$, and of its magnetic, $S_{s,mag}(\Omega_{subset})(\mathbf{r})$, and relaxation, $S_{s,relax}(\Omega_{subset})(\mathbf{r})$, components in the least-squares plane of the four ligand N atoms around each Cu^{II}. In the maps, {N1 + N1′}, {N2 + N2′} and {N3 + N3′} denote the subsets of the atoms of the system, including the bridging, the central and the terminal N atoms of the azido groups, respectively. The same colour codes and isovalue contours apply as in Fig. 1.

fifth panels in the first (CASSCF) and second (UB3LYP) rows of Fig. 5 reveal, respectively, the SF role played by all the N atoms of the system and that played by the N atoms of the azido ligands only. At the CASSCF(6,6) level, the N atoms act as diffuse negative sources, except for small regions of, higher in magnitude, positive SD around their nuclei. The diffuse negative sources are small but able to counteract the positive source from the Cu atoms in the region around N2 and in a tiny region between Cu and N1. There is also a noticeable counter effect of the pyridine N atoms on the positive sources around the N nuclei of the azido ligands. When only the {N$_{azido}$} sources are considered, the positive SD regions around their nuclei clearly increase in size. Conversely, at the UB3LYP level, the N atoms yield larger and definitely more delocalized regions of positive SD sources around their nuclei, with the positive sources around those of the azido ligands being scarcely affected by the presence or not of the sources from the pyridine N atoms. The two sets of N atoms appear to be more independent, relative to the CASSCF model, suggesting that higher delocalization of the unpaired electrons does not necessarily imply a greater connection between them. The positive SD sources around the Cu^{II}-bonded N are directed toward the Cu^{II} cation(s) they are linked to, thereby imparting a special split-lobe shape to the source of the bridging atoms of the azido ligands. The UB3LYP and CASSCF descriptions of the sources from the {N} and the {N$_{azido}$} subsets largely differ both for the SD source (Fig. 5) and for that of its magnetization and relaxation components (Fig. S2). The magnetic component imparts the shape of the SD sources at the UB3LYP level, while at the CASSCF level, the relaxation SD plays a more decisive role, especially for central and terminal atoms of the azido groups.
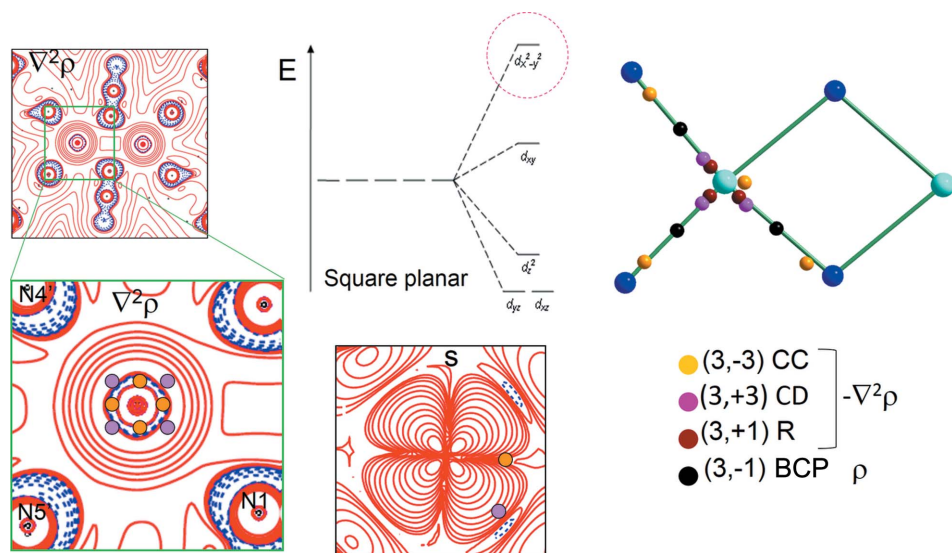
Fig. 6 enables one to distinguish neatly the different roles played by the bridging, the central and the terminal N atoms of the azido groups. The bridging atoms yield both local positive sources and diffuse negative sources, with a spin polarization mechanism of sources with its bonded atoms. The central atoms, instead, yield only diffuse negative sources and the terminal atoms diffuse and small positive sources. The source from the bridging N atoms is dominated by the magnetic component in both the CASSCF(6,6) and the UB3LYP calculations, but largely differs in shape and magnitude for the two models. The positive source around the N atom, directed towards the two linked metal atoms, is much larger in size at the UB3LYP level. On the contrary, the source from the central atoms is always dominated by the relaxation component, leading to an evident negative source for the SD. Both this component source and the SD source have a π-like shape. This is reminiscent of the symmetry of the unoccupied molecular orbitals (MOs) resulting from the mixing of the unoccupied π_u azido orbitals with the $d_{x^2-y^2}$ metal orbitals in a fragment orbital approach interpretation of the SD in the EO complex (Aebersold *et al.*, 1998). These MOs, unoccupied at the fragment orbital approach level, instead play a decisive role in the spin polarization mechanism within the azido ligand, when the system as a whole is considered (Aebersold *et al.*, 1998). Finally, for the terminal atoms, both density components are relevant and co-operate to make this atom act as a small positive source at both computational levels. Yet, CASSCF(6,6) predicts the relaxation component as more relevant, while it is the magnetic component that prevails at the UB3LYP level. To conclude, we observe that, except for a large part of the Cu-atom basins, the local SD is in general quite different from that due to the source of the closest atom or group of atoms, a difference which provides a local measure of the co-operating effects inherent to the electron spin delocalization and polarization mechanisms. In other words, except for Cu atoms, the sources of the other atoms in the systems are unable to explain, often even qualitatively, the SD distribution around them. The effect of other atoms is, in general, far from being negligible.

5.3. Cu^{II} 3d electron asphericity and its electron-density Laplacian and electron spin density image

In the EO complex, the Cu^{II} cation is *fourfold coordinated* in an almost *square-planar* arrangement of ligands. In this geometry and for a Cu^{II} cation (d^9 configuration), the $d_{x^2-y^2}$ orbital is the magnetic singly occupied orbital, according to crystal field theory (Fig. 7). The

Figure 7
Cu atom 3d electron asphericity and its electron-density Laplacian and electron spin density image in the end-on FM complex. Orbital ordering for a metal atom in a square-planar arrangement of ligands (top middle). The Laplacian of the CASSCF(6,6) electron density (top left) in the plane of the N atoms, with an enlargement (bottom left) of the VSCC and VSCD of Cu^{II}. CASSCF(6,6) spin density (bottom middle). The locations of the unique CPs of $-\nabla^2\rho$ and ρ, whose properties are reported in Table 2, are shown on the right of the figure. Locations of the charge concentrations (CC) and depletions (CD) are shown in the electron-density Laplacian and in the electron spin density maps around Cu^{II}.

Table 2

End-on (EO) FM complex: spin, $s(\mathbf{r})$, magnetic, $s_{mag}(\mathbf{r})$, relaxation, $s_{relax}(\mathbf{r})$, density and Laplacian of the electron density, $\nabla^2\rho(\mathbf{r})$, properties at bond critical points (BCPs) and at some relevant $-\nabla^2\rho$ critical points (CPs) along the Cu—Cu′, Cu—N1, Cu—N4 and Cu—N5 bonds.

CASSCF(6,6) data (UB3LYP data in parentheses); if not otherwise stated, all values are in atomic units.

Bond†	CP	R_{Cu}(Å)	$\nabla^2\rho(\mathbf{r})$	$s(\mathbf{r})$	$s_{mag}(\mathbf{r})$	$s_{relax}(\mathbf{r})$
Cu—Cu′	$-\nabla^2\rho$ (3,−3), CC	0.277 (0.278)	−104.95 (−94.76)	0.000 (0.011)	0.000 (0.000)	0.000 (0.011)
Cu—N1	$-\nabla^2\rho$ (3,+3), CD	0.429 (0.434)	19.33 (18.04)	0.413 (0.278)	0.412 (0.274)	0.001 (0.004)
	$-\nabla^2\rho$ (3,+1), R	0.292 (0.288)	−28.37 (−41.13)	1.030 (0.750)	1.029 (0.733)	0.001 (0.017)
	$-\nabla^2\rho$ (3,−3), CC	1.624 (1.606)	−2.07 (−1.77)	0.005 (0.019)	0.006 (0.019)	−0.001 (0.000)
	ρ, BCP	0.939 (0.967)	0.36 (0.28)	0.007 (0.002)	0.007 (0.003)	0.000 (−0.001)
Cu—N4	$-\nabla^2\rho$ (3,+3), CD	0.430 (0.434)	19.41 (18.13)	0.416 (0.286)	0.416 (0.282)	0.000 (0.004)
	$-\nabla^2\rho$ (3,+1), R	0.292 (0.288)	−29.27 (−42.04)	1.051 (0.792)	1.050 (0.774)	0.001 (0.018)
	$-\nabla^2\rho$ (3,−3), CC	1.597 (1.595)	−2.74 (−2.38)	0.008 (0.036)	0.008 (0.032)	0.000 (0.004)
	ρ, BCP	0.925 (0.954)	0.39 (0.28)	0.007 (0.001)	0.007 (0.002)	0.000 (-0.001)
Cu—N5	$-\nabla^2\rho$ (3,+3), CD	0.429 (0.434)	19.48 (18.17)	0.418 (0.284)	0.418 (0.280)	0.000 (0.004)
	$-\nabla^2\rho$ (3,+1), R	0.292 (0.288)	−28.87 (−41.96)	1.057 (0.788)	1.056 (0.770)	0.001 (0.018)
	$-\nabla^2\rho$ (3,−3), CC	1.593 (1.591)	−2.69 (−2.35)	0.008 (0.033)	0.008 (0.030)	0.000 (0.003)
	ρ, BCP	0.923 (0.953)	0.39 (0.29)	0.008 (0.001)	0.008 (0.002)	0.000 (−0.001)

† $-\nabla^2\rho$ CP legend: (3,−3) charge concentration, CC; (3,+3) charge depletion, CD; (3,+1) ring, R.

topology of the Laplacian of the electron density may validate whether such a simplified model theory is also reflected in the properties of an observable (Gatti, 2005). In particular, the asphericity of the 3d electron distribution around a metal atom, due to an unequal occupation of its 3d valence orbitals, may be neatly revealed this way (Bianchi *et al.*, 1996; Macchi & Sironi, 2003; Gatti, 2005; Lo Presti & Destro, 2008). Topological analysis of $-\nabla^2\rho$ in the valence-shell charge concentration (VSCC; Bader, 1990) and valence-shell charge depletion (VSCD; Bader, 1990) regions of the Cu atoms finds four (3,+3) $-\nabla^2\rho$ minima, *i.e.* charge depletions (CDs), lying almost on the Cu—N_{py} and on the Cu—$N_{bridging}$ internuclear axes and four (3,−3) $-\nabla^2\rho$ maxima, *i.e.* charge concentrations (CCs), lying in between the CDs (Fig. 7).

Thus, the CDs, located at 0.27 Å from the Cu nucleus, may be associated with the lobes of the formally singly occupied $d_{x^2-y^2}$ orbital and the CCs, located at 0.43 Å from the Cu nucleus, with the lobes of the formally doubly occupied d_{xy} orbital. If such an association is plausible, one would anticipate a large SD value at the CDs and much smaller values at the CCs. Conversely, CDs should be characterized by positive and low $\nabla^2\rho$ values compared with the high $|-\nabla^2\rho|$ magnitudes at CCs, illustrating that the electron-density Laplacian and the electron SD distributions provide complementary pictures. Where one scalar field is concentrated, the other is depleted and *vice versa*, since a higher SD value implies a region dominated by a metal orbital with low electron occupation, while a higher CC, hence a higher $|-\nabla^2\rho|$ magnitude, implies a region dominated by a metal orbital with higher or maximal orbital occupation.

The results shown in Table 2 neatly confirm our hypothesis. For instance, at the CASSCF(6,6) level, the s and $\nabla^2\rho$ values are 0.413 and 19.33 a.u. at the CD along the Cu—N1 axis, relative to the 0.001 and −104.95 a.u. values at the CC lying along the Cu—Cu′ axis. Qualitatively similar results are found at the UB3LYP level (Table 2), but the s values (0.278 and 0.011 a.u.) are decreased at the CD and significantly increased at the CC, with respect to the electron-correlated wavefunc-

tion. High SD at the CDs is almost all due to the magnetic term, while the very low SD at the CCs has essentially a relaxation density origin (Table 2). Since the UB3LYP model exaggerates both the spin delocalization to the ligands and the local spin relaxation mechanisms, SD turns out to be smaller at CDs and larger at CCs close to the Cu nucleus, relative to the CASSCF(6,6) values. A (3,+1) $-\nabla^2\rho$ ring (R, Table 2) critical point is also found along all the Cu—N_{ligand} axes and located at a distance from the Cu nucleus very close (0.28 Å) to that of the CCs. At this point, the $\nabla^2\rho$ is negative, as at the CC *rp*, but significantly lower in magnitude, while the SD is extremely large [for instance, $\nabla^2\rho = -28.37$ a.u. and $s = 1.030$ a.u. at the ring point along Cu—N1, at the CASSCF(6,6) level]. This ring CP region is also associated with the $d_{x^2-y^2}$ orbital. These additional data further corroborate our analysis relating Cu metal asphericity with the SD and the Laplacian of electron-density features around the metal. It is also worth noting that both the SD and the SD Laplacian portraits of the Cu^{II} cation provide a rigorous *picture* of an orbital density, one based on quantum observables and not on a model.

Also reported in Table 2 are the s and $\nabla^2\rho$ values at the Cu—N BCP locations and at the CCs lying in the VSCCs of the pyridine and bridging N atoms. These CCs, one for each N atom except for N1, which has two equivalent CCs of this kind, are all almost aligned in a *key–lock* arrangement, with the corresponding CDs located close to the Cu nucleus. At the CASSCF(6,6) level, the SD at the N-atom CCs and at the Cu—N BCP locations is low, about two orders of magnitude lower than at the Cu CDs and essentially due to the magnetic component (Table 2). On the other hand, UB3LYP predicts SD values that are three times higher at the N-atom CCs and half as high at the BCPs, relative to CASSCF(6,6). Yet, also for the UB3LYP model, the SD at these critical points is largely dominated by the magnetic component (Table 2). Note that all UB3LYP Cu—N BCP locations are displaced towards the N nuclei, relative to the CASSCF(6,6) wavefunction. This fact corroborates the link between the UB3LYP excessive spin delocalization to ligands and the decreased dative or increased
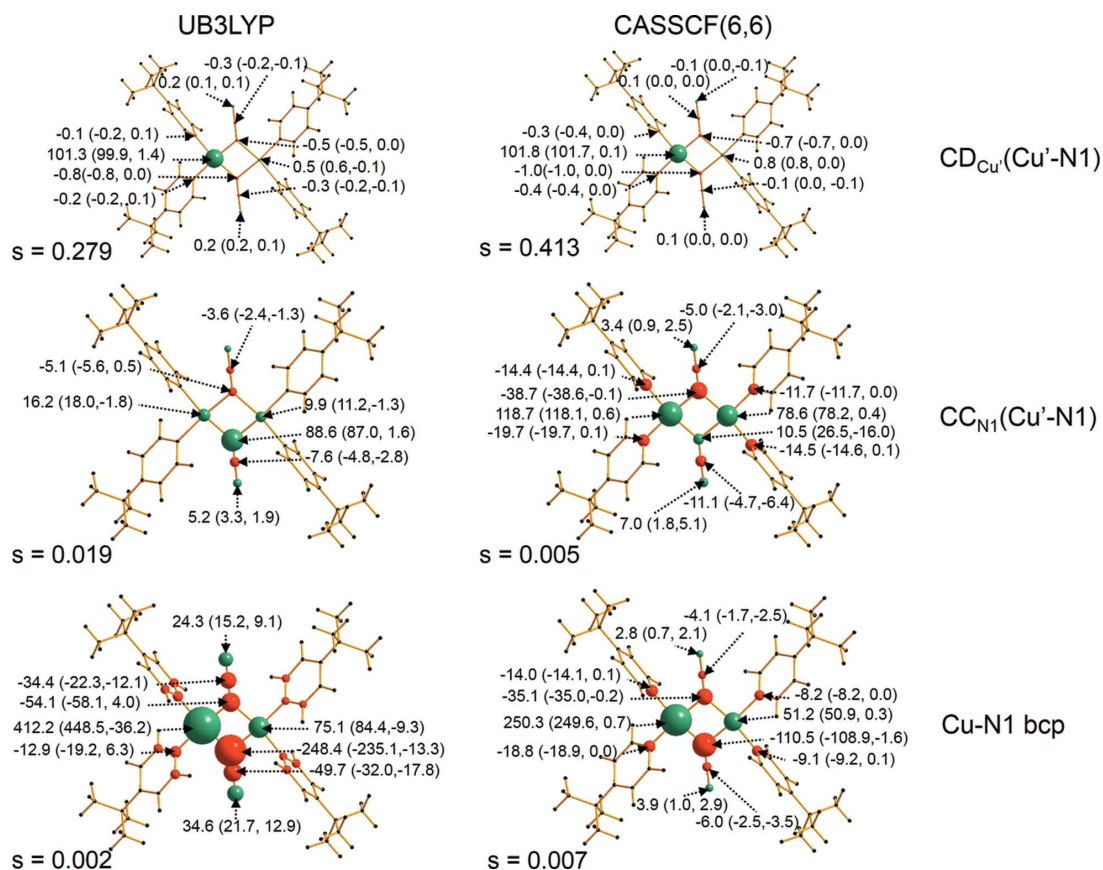
Figure 8
End-on FM complex: UB3LYP and CASSCF(6,6) SF percentage contributions to the electron spin density s (magnetic and relaxation components in parentheses) at selected reference points, rps (Table 2). Rps: $CD_{Cu'}(Cu'-N1)$ denotes the charge depletion in the valence-shell charge depletion (VSCD) of the Cu′ atom and lying along Cu′−N1, while $CC_{N1}(Cu'-N1)$ denotes the charge concentration in the valence-shell charge concentration (VSCC) of the N1 atom and lying almost along Cu′−N1. The reported s values at rps are in a.u. Green (red) atomic balls denote an α (β) effect on the spin density at the reference point. SF percentage contributions are positive or negative whether they concur or oppose to reconstruct the corresponding spin density value at the rp.

covalent character of the Cu−N bonding, leading to a smaller positive charge on Cu and to the BCP displacement towards N atoms.

5.4. Source Function analysis at selected reference points

In §5.2, spin, magnetic and relaxation densities in the EO complex have been shown and the way these densities are determined from their atomic or atomic group sources, in the plane of the N-atom ligands around the Cu^II atom, has been discussed. In §5.3, the relationship between Cu^II 3d electron asphericity and features of the electron-density Laplacian and electron SD around this atom have been pointed out. Properties at a number of peculiar molecular points have been analysed and some of those points are now considered as convenient rps for a conventional SF spin density analysis, along with Cu′, N1 and N4′ nuclei as additional rps (Figs. 8 and 9). Let us first consider atomic sources at the CD in the VSCD of Cu′ along Cu′−N1 [$CD_{Cu}(Cu'-N1)$ in Fig. 8]. SD is dominated by the source of Cu′ (101.8 and 101.3% at the CASSCF and UB3LYP levels, respectively) and essentially by its magnetic component (101.7 and 99.9% at the CASSCF and UB3LYP levels, respectively). Yet, despite being very small in percentage, sources from the atoms of the azido ligands (in particular atom N1) and from the remote Cu atom are not negligible in absolute value and being negative, except those from Cu and from the terminal atoms of the azido ligands, contrast the source from Cu′. A |1%| value for such contributions amounts to |0.003| a.u. (UB3LYP), which is, for instance, larger than the value (0.002 a.u.) of the total SD at Cu′−N1 BCP and a typical SD value in many regions of the system. These sources, in an analogous manner to the dominant one from Cu′, are essentially due to the magnetic component. Their absolute value assesses the local importance of the spin back-delocalization mechanism from the ligands to the paramagnetic centre or, in the case of Cu, the spin delocalization between the paramagnetic centres themselves. Then, being the SD positive at the rp, their positive (α effect) or negative (β effect) sign determines whether they concur or contrast the SD at this CD. Interestingly, the remote Cu, at variance with the bridging N atoms, concurs with the SD at the Cu′ CD, in agreement with the two Cu^II cations being ferromagnetically coupled through the magnetic density.

It is interesting to compare the SF pattern at the CD in the VSCD of Cu′ along Cu′−N1 with that at the CC along Cu′−

Cu and close to Cu′ (not shown in the figure). As discussed earlier, the SD here is almost zero [−0.00005 a.u., CASSCF(6,6)] or small [0.011 a.u., UB3LYP] and with a non-null relaxation component only. However, such a negligible or small value is, for both methods, the result of a perfect balance among relatively high magnetic sources that oppose each other to yield an overall null magnetic source. Both Cu atoms play an α effect, while the bridging and central N atoms of the azido ligands and the pyridine N atoms oppose them with a β effect almost equal in magnitude. Overall, at an rp related to the magnetic pathway [$i.e.$ at $CD_{Cu}(Cu′−N1)$], the magnetic sources dominate and the SD is large, while at one related to a doubly occupied orbital ($i.e.$ the CC along Cu′−Cu; Table 2) the magnetic sources, despite being relatively high and definitely much more delocalized, cancel each other. As a result, the SD is small here and tends to zero when a properly correlated method is adopted.

The SD at the CC along Cu′−N1 and close to N1 is low [0.019 and 0.005 a.u. at the UB3LYP and CASSCF(6,6) levels, respectively] compared with that at the facing CD in the VSCD of Cu′ along Cu′−N1, but still relevant, especially at the UB3LYP level. Its pattern of sources is very revealing (Fig. 8). The N1 bridging atom and the two Cu atoms all co-operate with their α effect to the positive SD at the rp, while N1′ and all other N atoms of the pyridine ligands tend to contrast this SD accumulation with their clear β effect. This behaviour highlights the co-operative mechanisms, acting at the rp, in

favour or against spin delocalization from one paramagnetic to the other paramagnetic centre through the bridging N1 atom of the azido ligand. All sources of atoms along this ferromagnetic pathway concur, while those related to atoms linked through other magnetic pathways are working against. As expected, being related to the spin delocalization mechanism, the SF pattern is here essentially determined by the magnetic component. The UB3LYP and CASSCF(6,6) methods agree qualitatively in their description, but largely differ from a quantitative point of view. Since the UB3LYP method exaggerates spin delocalization to the ligands, it also predicts a larger positive source from N1 than from the two paramagnetic centres, while these latter dominate the CASSCF(6,6) description. CASSCF(6,6) also gives a much larger relative weight to the opposing effect from sources related to the atoms of the non-directly involved magnetic pathways. Once more we find that a larger spin delocalization to ligands (UB3LYP method) does not imply a relatively larger SF communication among the network of atoms involved in the spin delocalization.

In terms of an orbital language, the positive SD region around the bridging N (where its lone pair CCs are located), pointing towards the Cu^{II} cations, may be explained in two ways. Either in terms of spin delocalization through the mixing of the Cu $d_{x^2−y^2}$ orbitals and the π $gerade$ and π $ungerade$ orbitals of the azido ligands (Aebersold et $al.$, 1998) or also in terms of a superexchange mechanism between the two Cu^{II}
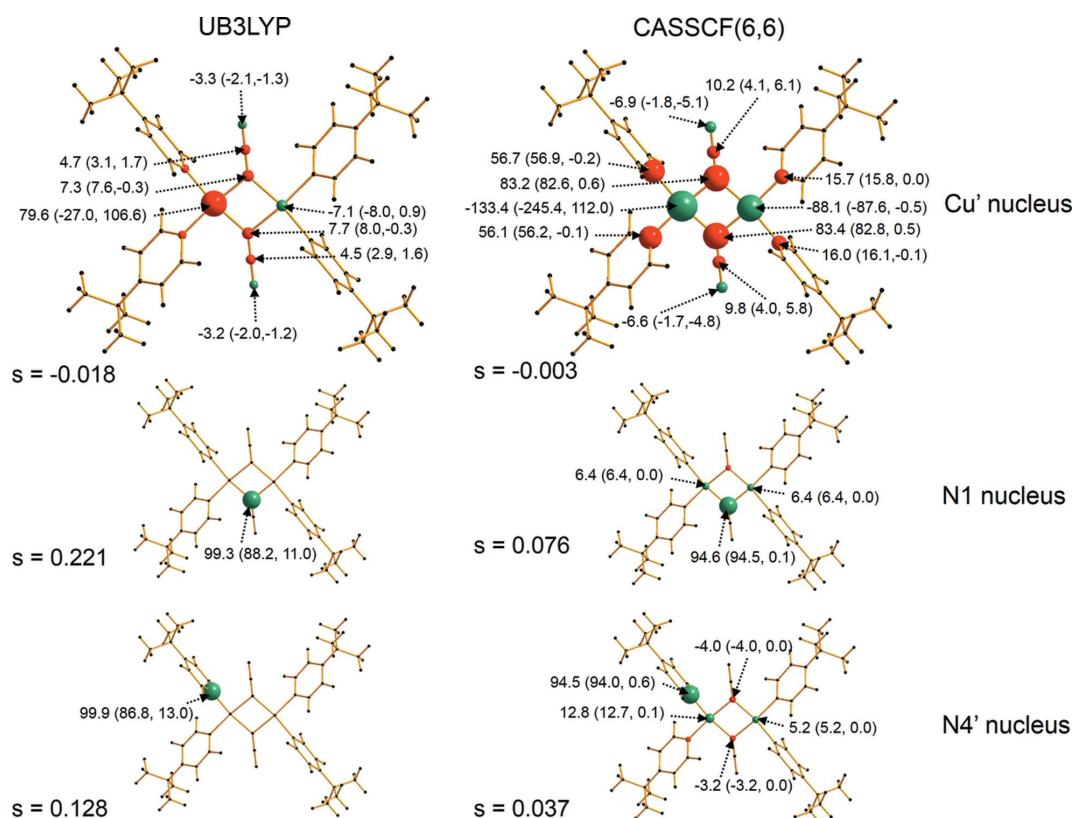

Figure 9
End-on FM complex: UB3LYP and CASSCF(6,6) SF percentage contributions to the s (magnetic and relaxation components in parentheses) at selected nuclear positions. The s values at rps are in a.u. Green (red) atomic balls denote an α (β) effect on the density at the reference point. SF percentage contributions are positive or negative whether they concur or oppose to reconstruct the corresponding density value at the indicated nucleus.

cations and the intervening bridging N1 atom, when this latter subtends an angle of about 90° (Elliott, 1998). In such a case, ferromagnetic coupling is favoured due to the mixing with an excited configuration having two unpaired electrons in different and orthogonal orbitals on the bridging atom, and whose associated densities are reminiscent of the shape of the positive SD region found around the bridging N. While these are just orbital models, the SF analysis provides a rigorous picture of such orbital interaction mechanisms at the N1 CC in terms of delocalized and co-operating sources along the Cu′—N1—Cu pathway.

Fig. 8 also shows the atomic SF spin density pattern for an rp taken at the Cu′—N1 BCP. SD is here small and positive [0.002 and 0.007 a.u. at the UB3LYP and CASSCF(6,6) levels, respectively]. It is over-determined by the magnetic (positive) and opposed by the relaxation (negative) SD components, the former essentially due to the source from the Cu′ atom and the latter largely due to the sources from the bridging and central atoms of the azido ligands (Figs. 5 and 6). The magnetic source from these N atoms also yields a β effect at the BCP. Therefore, SF contributions from the bonded Cu′ and N1 atoms are clearly opposite in sign, i.e. α for Cu′ and β for N1. At the UB3LYP level, these SF contributions are respectively four and two times larger in magnitude than the SD they contribute to reconstruct [two and half this magnitude and the same magnitude of the SD at the CASSCF(6,6) level, respectively]. Opposing sources from the bonded atoms imply that a spin polarization mechanism operates in the bonding region at the BCP; however, with the sources being still essentially due to the magnetic component, especially at the CASSCF(6,6) level. One notices that there are large contributions from all the N of the azido ligands and also from the other Cu atom, which, differently from N1′, co-operates with Cu′ in determining the positive SD at the Cu′—N BCP.

Fig. 9 shows the SF spin density reconstruction at the Cu′, N1 and N4′ nuclei. At the N1 nucleus, the SD is very large [0.221 and 0.076 a.u. at the UB3LYP and CASSCF(6,6) levels, respectively] and essentially due to the magnetic component at the CASSCF(6,6) level, while at the UB3LYP level also the relaxation density co-operates. The three-times-larger SD at the UB3LYP level results from the observed exaggeration of spin delocalization on ligands by this model. However, while at the UB3LYP level the SD at the N1 nucleus is almost only due to the source from its own atom, the CASSCF(6,6) model highlights the role of the co-operating α sources from the two Cu atoms, able to cause 13% of the SD at the N1 nucleus. Again, the UB3LYP model exaggerates the amount of spin delocalization on the ligands and underestimates spin *connection* or *communication* mechanisms. Similar observations may be made for the reconstruction of the SD at the N4′ nucleus. At the CASSCF(6,6) level, both Cu′ (12.8%) and the remote Cu atom (5.2%) co-operate with the N4′ atom (94.5%) in determining a significant SD (0.037 a.u.) on the N4′ nucleus, while such a mechanism is totally absent at the UB3LYP level, despite a three-times-larger SD at its nucleus (0.128 a.u.). SD at the Cu′ nucleus is negative and close to zero (−0.003 a.u.) at the CASSCF(6,6) level, while it is six times larger in magnitude (−0.018) at the UB3LYP level. The two methods predict quite different patterns of sources. The relatively large SD at the UB3LYP level is probably due to the limits of such a model.

Indeed, at the CASSCF(6,6) level, the marginal negative SD at Cu′ is due to an almost perfect balance between large opposing α effects from the two Cu atoms and negative delocalized sources from the other atoms. Looking in more detail, the sources of all atoms are almost due only to the magnetic component of the SD, except for Cu′, for which the relaxation component also plays a major role.

Fig. S3 of the supporting information reports SF patterns for rps along Cu′—N4′ corresponding to those along Cu′—N1 shown in Fig. 8. These patterns all closely resemble those already discussed for rps along Cu′—N1 and may be similarly interpreted.
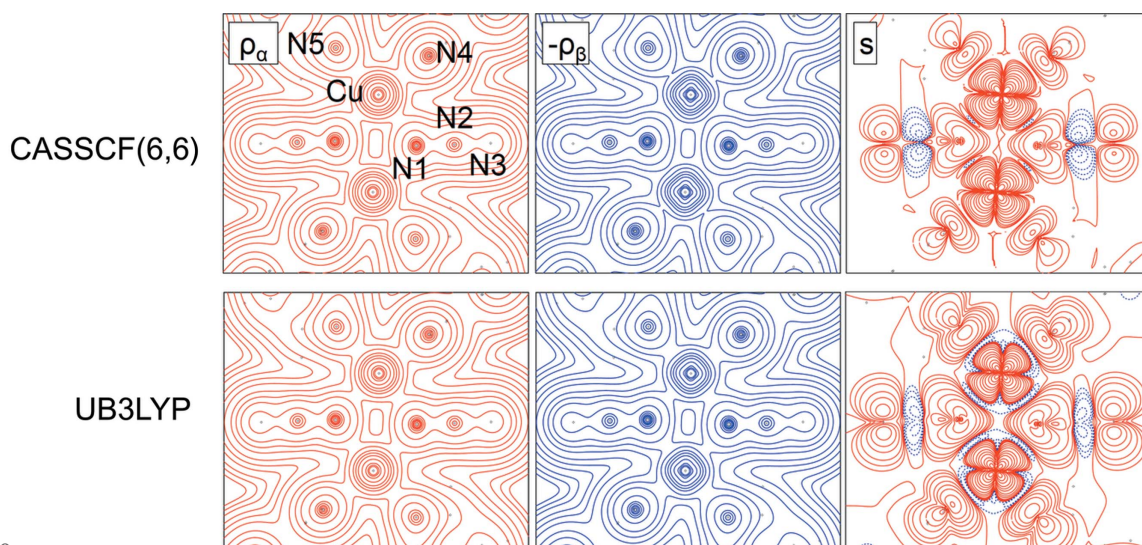

Figure 10
End-on (EO) FM complex: CASSCF(6,6) and UB3LYP contour plots of spin-resolved, ρ_α, $-\rho_\beta$ electron densities and of electron spin density $s = \rho_\alpha - \rho_\beta$, in the least-squares plane of the four ligand N atoms around each Cu^{II}. The same colour codes and isovalue contours occur as in Fig. 1.

5.5. Comparing spin-resolved components *versus* spin densities: a test for the model quality

We have thus far analysed spin densities and their Laplacian, but not their spin-resolved ρ_α and ρ_β components, as performed by Deutsch *et al.* (2014), using a split-spin multipolar model to jointly refine X-ray and PND data. For the EE complex, Deutsch *et al.* (2014) reported a fair agreement between the so-obtained spin-resolved components and those estimated using a UB3LYP DFT approach. A question that needs to be addressed before concluding is whether an agreement on the spin-resolved components obtained by two different approaches also ensures a similar agreement of their resulting SDs. Fig. 10 compares contour plots of ρ_α, $-\rho_\beta$ and of their sum, the spin density $s = \rho_\alpha + (-\rho_\beta)$, for the EO complex evaluated at the CASSCF(6,6) and at the UB3LYP levels. Contour plots are drawn in the least-squares plane of the four ligand N atoms around each Cu^{II} (see Fig. 2). The spin-resolved components appear to be similarly described by the two considered methods. In particular, ρ_α has a circular shape around the Cu nucleus, whereas ρ_β has the rounded square shape one anticipates for an incomplete filling of the Cu $d_{x^2-y^2}$ orbital, with CDs along the Cu^{II}-to-ligand bonds and CCs between adjacent CDs. In other words, the α electrons (almost) completely fill the five d α-spin orbitals on Cu, while the minority β-spin electrons incompletely fill the β-spin orbitals, leading to the discussed CDs and CCs around the Cu nucleus. On the other hand, noticeable qualitative differences may be observed between the SDs maps obtained at the CASSCF(6,6) and at the UB3LYP levels, *despite the evident similarities between their spin-resolved components*. As discussed earlier, a much larger spin delocalization to the ligands, along with the consequent lower SD around Cu^{II} and the negative SD region at its boundaries is visibly manifested in the UB3LYP map. The qualitative shape of the α and β components is imparted by all their electrons, the majority of them being described quite similarly in the two distributions as they fill doubly occupied orbitals. Comparison of the spin density, instead, singles out the difference between the distributions of only those few electrons that are either missing in the minority spin distribution or are described in a significantly different manner by the spin-resolved distributions. Different model approaches may significantly differ in the description of, namely, such few peculiar electrons.

A similar analysis was performed for the case of the EE complex. As shown in Fig. S4, the CASSCF(6,6) and UB3LYP contour plots of spin-resolved electron densities, in the least-squares plane of the Cu—O bond and of the three shorter Cu—N bonds, are almost indistinguishable, while those of the corresponding SDs largely differ. Our spin-resolved components also mostly agree (Fig. S4) with those obtained by Deutsch *et al.* (2014) from either the joint refinement of X-ray and PND data or the UB3LYP calculation (minor differences may be ascribed to the different choice of contour levels). Yet this does not imply similar SDs and atomic SD populations, as demonstrated here for the EO complex. Results for the EE complex, with a change of method, follow the same trends

discussed for the EO system and will be illustrated in future work.

6. Conclusions

Magnetic interactions between metal atoms, mediated through diamagnetic ligands acting as couplers, are customarily discussed in terms of superexchange interactions and of spin delocalization and polarization mechanisms. Orbital models (Aebersold *et al.*, 1998; Aronica *et al.*, 2007; Dos Santos *et al.*, 2016) and/or topological analyses of the spin density (Dos Santos *et al.*, 2016) are used to interpret the spin density (SD) distribution and obtain further insight on such interactions and mechanisms.

In this work, we applied the Source Function (SF) tool to the analysis of the SD in an azido Cu^{II} dinuclear complex, where magnetic interactions between the metal atoms take place through the azido ligands, coordinated in an end-on mode, and also through the external pyridine ligands. Firstly, a clear relationship between the electron-density Laplacian and the SD distribution around the metal atom has been established. Then, application of the SF tool has enabled us to highlight how the magnetic centres contribute to determine the local spin delocalization and polarization at any point of the complex and whether a given atom or group of atoms of the ligands is co-operating in favour or against a certain local spin delocalization/polarization. This SF capability provides an unprecedented atomic insight on SD distributions and on the local role played by the remote or closer atomic centres, within a cause–effect view.

Reconstruction of partial SDs by means of the Source Function has been introduced for the first time. This reconstruction enables us to visualize, simultaneously, the mechanisms and effects discussed earlier, at all points of space or in selected molecular planes, and for a specific subset of contributing atoms. When all atoms of a system are included in such a subset, one is then led back to the conventional SD analysis. Partial SDs also permit an easier interpretation of the usual SF percentage reconstructions at given reference points and provide invaluable help for an appropriate choice of such points. The ball-and-stick representations of these zero-dimensional SF reconstructions, allow for a visualization of the magnetic pathways and of the specific role played by each atom along these paths. Decomposition of SF contributions in terms of a magnetic and of a relaxation component provides further insight for all kinds of adopted SF representation (zero- and two-dimensional in the present study).

SD distributions may largely depend on the way they are calculated from *theoretical* approaches or are derived from diffraction experiments. In the present study, the SF analysis has neatly identified the similarities and differences between SD distributions obtained from a standard unrestricted DFT method, using an exchange correlation functional of the hybrid type (UB3LYP), or from a more costly and accurate CASSCF approach. UB3LYP greatly overestimates spin delocalization to the ligands, while comparatively underestimating magnetic connection (*spin transmission*) among

atoms, along the magnetic pathways. Because of the excessive spin delocalization, the UB3LYP method is forced to introduce or to overestimate spin polarization mechanisms between the paramagnetic centres and the ligands, leading to an exaggerated partial covalent nature of metal–ligand interactions which eventually dampens spin transmission. Decomposition in a magnetic and in a relaxation component provides further understanding of the origin of the observed SD discrepancies. Spin delocalization from PND data seems intermediate in its extent between that calculated at the UB3LYP and at the CASSCF levels. The SF tool, when applied to *ab initio* SDs and to those derived from experiment, could be of great value for a better understanding of the very origin of differences. Use of a high-quality wavefunction seems to be required when comparing theoretical and experimentally derived (PND) spin densities. Despite the very small number of normally available PND structure-factor data and despite the consequent adoption of very rigid models in their refinement, SDs derived this way appear in general superior to those obtained through a DFT UB3LYP approach and closer to the far more accurate CASSCF result. The relevance of the experimentally derived SDs is further manifest when considering the difficulty in reaching a reasonable convergence of CASSCF estimates against the number of correlated electrons even for systems of a moderate size.

We also showed that a visual, almost perfect, agreement on the spin-resolved electron densities (ρ_α and ρ_β), obtained from different approaches, does not yet ensure a corresponding agreement between their associated SDs. Lots of fundamental details and significant differences may indeed emerge from their direct comparison.

References

Aebersold, M., Gillon, B., Plantevin, O., Pardi, L., Kahn, O., Bergerat, P., von Seggern, I., Tuczek, F., Öhrström, L., Grand, A. & Lelièvre-Berna, E. (1998). *J. Am. Chem. Soc.* **120**, 5238–5245.

Arfken, G. (1985). *Mathematical Methods for Physicists.* Orlando: Academic Press.

Aronica, C., Jeanneau, E., El Moll, H., Luneau, D., Gillon, B., Goujon, A., Cousson, A., Carvajal, M. A. & Robert, V. (2007). *Chem. Eur. J.* **13**, 3666–3674.

Bader, R. F. W. (1990). *Atoms in Molecules: A Quantum Theory.* Oxford University Press.

Bader, R. F. W. & Gatti, C. (1998). *Chem. Phys. Lett.* **287**, 233–238.

Bianchi, R., Gatti, C., Adovasio, V. & Nardelli, M. (1996). *Acta Cryst.* B**52**, 471–478.

Biegler-König, F. W., Bader, R. F. W. & Tang, T.-H. (1982). *J. Comput. Chem.* **3**, 317–328.

Boguslawski, K., Jacob, C. R. & Reiher, M. (2011). *J. Chem. Theory Comput.* **7**, 2740–2752.

Boguslawski, K., Marti, K. H., Legeza, O. & Reiher, M. (2012). *J. Chem. Theory Comput.* **8**, 1970–1982.

Conradie, J. & Ghosh, A. (2007). *J. Phys. Chem. B*, **111**, 12621–12624.

Coppens, P. (1997). *X-ray Charge Densities and Chemical Bonding.* Oxford University Press.

Coppens, P. (2009). *Angew. Chem. Int. Ed.* **48**, 4280–4281.

Coppens, P. (2015). *Phys. Scr.* **90**, 058001.

Deutsch, M., Claiser, N., Pillet, S., Chumakov, Y., Becker, P., Gillet, J.-M., Gillon, B., Lecomte, C. & Souhassou, M. (2012). *Acta Cryst.* A**68**, 675–686.

Deutsch, M., Gillon, B., Claiser, N., Gillet, J.-M., Lecomte, C. & Souhassou, M. (2014). *IUCrJ*, **1**, 194–199.

Dos Santos, L. H. R., Lanza, A., Barton, A. M., Brambleby, J., Blackmore, W. J. A., Goddard, P. A., Xiao, F., Williams, R. C., Lancaster, T., Pratt, F. L., Blundell, S. J., Singleton, J., Manson, J. L. & Macchi, P. (2016). *J. Am. Chem. Soc.* **138**, 2280–2291.

Elliott, S. R. (1998). *The Physics and Chemistry of Solids.* Chichester: John Wiley and Sons.

Farrugia, L. J., Evans, C. & Tegel, M. (2006). *J. Phys. Chem. A*, **110**, 7952–7961.

Frisch, M. J. *et al.* (2009). *GAUSSIAN*09, Revision A.1. Gaussian, Inc., Wallingford, CT, USA.

Gatti, C. (2005). *Z. Kristallogr.* **220**, 399–457.

Gatti, C. (2012). *Struct. Bonding*, **147**, 193–286.

Gatti, C. (2013). *Phys. Scr.* **87**, 048102.

Gatti, C., Cargnoni, F. & Bertini, L. (2003). *J. Comput. Chem.* **24**, 422–436.

Gatti, C. & Lasi, D. (2007). *Faraday Discuss.* **135**, 55–78.

Gatti, C. & Macchi, P. (2012). *Modern Charge Density Analysis*, edited by C. Gatti and P. Macchi, ch. 1, pp. 1–78. Dordrecht, Heidelberg, London, New York: Springer.

Gatti, C., Orlando, A. M. & Lo Presti, L. (2015). *Chem. Sci.* **6**, 3845–3852.

Gatti, C., Orlando, A. M., Monza, E. & Lo Presti, L. (2016). *Applications of Topological Methods in Molecular Chemistry*, edited by R. Chauvin, C. Lepetit, B. Silvi & E. Alikhani, Vol. 22, ch. 5, pp. 101–129. Switzerland: Springer International Publishing.

Gatti, C., Saleh, G. & Lo Presti, L. (2016). *Acta Cryst.* B**72**, 180–193.

Gillet, J.-M. (2007). *Acta Cryst.* A**63**, 234–238.

Gillet, J.-M., Becker, P. J. & Cortona, P. (2001). *Phys. Rev. B*, **63**, 235115, 1–7.

Gillet, J.-M. & Koritsanszky, T. (2012). *Modern Charge Density Analysis*, edited by C. Gatti & P. Macchi, ch. 5, pp. 181–211. Dordrecht, Heidelberg, London, New York: Springer.

Gillon, B. & Becker, P. (2012). *Modern Charge Density Analysis*, edited by C. Gatti & P. Macchi, ch. 8, pp. 277–302. Dordrecht, Heidelberg, London, New York: Springer.

Gillon, B., Sangregorio, C., Caneschi, A., Gatteschi, D., Sessoli, R., Ressouche, E. & Pontillon, Y. (2007). *Inorg. Chim. Acta*, **360**, 3802–3806.

Hansen, N. K. & Coppens, P. (1978). *Acta Cryst.* A**34**, 909–921.

Herzberg, G. (1966). *Molecular Spectra and Molecular Structure. III. Electronic Spectra and Electronic Structure of Polyatomic Molecules.* New York: Van Nostrand Reinhold Company.

Koritsanszky, T. S. & Coppens, P. (2001). *Chem. Rev.* **101**, 1583–1627.

Lo Presti, L. & Destro, R. (2008). *J. Chem. Phys.* **128**, 044710.

Macchi, P., Gillet, J.-M., Taulelle, F., Campo, J., Claiser, N. & Lecomte, C. (2015). *IUCrJ*, **2**, 441–451.

Macchi, P. & Sironi, A. (2003). *Coord. Chem. Rev.* **238–239**, 383–412.

Peintinger, M. F., Oliveira, D. V. & Bredow, T. (2013). *J. Comput. Chem.* **34**, 451–459.

Pendás, A. M., Francisco, E., Blanco, M. A. & Gatti, C. (2007). *Chem. Eur. J.* **12**, 9362–9371.

Ponec, R. & Gatti, C. (2009). *Inorg. Chem.* **48**, 11024–11031.

Putz, H. & Brandenburg, K. (1997–2012). *DIAMOND.* Crystal Impact GbR, Bonn, Germany.

Stewart, R. F., Bentley, J. & Goodman, B. (1975). *J. Chem. Phys.* **63**, 3786–3793.

Volkov, A. V., Macchi, P., Farrugia, L. J., Gatti, C., Mallinson, P., Richter, T. & Koritsanszky, T. (2006). *XD*2006. University at Buffalo, State University of New York, NY, USA; University of Milano, Italy; University of Glasgow, UK; CNR–ISTM, Milano, Italy; Middle Tennessee State University, TN, USA.